國立臺灣大學理學院氣候變遷與永續發展國際學位學程

碩士論文

International Degree Program in Climate Change and Sustainable Development

College of Science

National Taiwan University

Master Thesis

屋頂型光伏太陽能板對局部環流與對流潛在的影響

The Potential Impact of Rooftop Solar Photovoltaic Installation on

Local Circulation and Convection in Taipei

張博深

Po-Shen Chang

指導教授：陳正平 博士、謝正義 博士

Advisor: Jen-Ping Chen, Ph.D. & Cheng-I Hsieh, Ph.D.

中華民國 109 年 7 月

July, 2020

中文摘要

　　本研究探討屋頂型光伏太陽能板對局部環流與對流潛在的影響。在擁擠的都市地區，屋頂型光伏太陽能提供了一個有效率的空間使用方案。然而隨著裝設的規模愈來愈大，對於環境可能會造成意料之外的影響。太陽能板會改變地表的輻射收支，進而可能會增強或減弱都市熱島效應，又都市熱島效應已有不少研究指出，會對台灣的午後對流產生影響，因此，太陽能板所造成的溫度改變可能也會進一步的影響局部環流與對流。本研究以都會區台北市為例，以數值模擬實驗測試不同的太陽能轉換效率對環境可能產生的影響。結果顯示，光伏太陽能會在台北市產生冷島效應，增加台北市與南方山區的溫度梯度，進而有較強的氣流沿著山脈爬升，導致在較高海拔較早開始產生對流，進而使降雨區往山區移動。在都市方面，因為冷島效應提供較穩地的大氣環境，進而產生一阻擋效應，使對流較不易移入台北市，因此在台北市有較強的降雨減少訊號。太陽能的轉換效率愈高，冷島效應也會愈強，降雨的改變也愈明顯。

關鍵字：光伏太陽能、局部環流、午後對流、降雨、數值實驗

ABSTRACT

This study investigated the potential impact of rooftop solar photovoltaic (PV) installation on local circulation and convection in the urban area. The rooftop solar PV system is a space-efficient option to deploy renewable energies in the crowded urban area. However, as the installation scale increases, the unintentional impact on local climate may emerge. In particular, PV array deployment can change the surface radiative balance and thus enhance or reduce the urban heat island (UHI) effect. The UHI effect has been implicated to influence afternoon thunderstorm activities in the tropical island, Taiwan. Therefore, temperature change due to PV installation may also alter the local circulation and convection. This research takes the Taipei City, which is a metropolitan area in northern Taiwan, for a case study. Citywide rooftop solar PV installation experiments are conducted by using the Weather Research and Forecasting (WRF) Model coupled with an urban canopy model. Different PV conversion efficiency scenarios, including current and future technology levels, are simulated to evaluate the potential impact of solar PV installation.

The results show that solar PV would cause a cold island effect (CIE) in the Taipei City. The CIE would increase the temperature gradient between the Taipei City and the mountains south of the Taipei Basin. This circulation change results in a stronger upslope flow such that the heavy-rainfall region shifted upslope, which can trigger the convection to occur earlier at higher altitudes. On the city side, the strength of heavy precipitation decreased because of the blocking effect of colder air, which causes a more stable environment over the Taipei City. Such effects are stronger for higher PV energy conversion efficiency, including a stronger CIE and more obvious precipitation change.

Keywords: Solar Photovoltaic, local circulation, afternoon convection, rainfall, numerical simulation.

CONTENTS

LIST OF FIGURES

v

Chapter 1　Introduction

Recently, owing to the rising awareness of global warming and reducing carbon dioxide (CO_2) emission, the energy issue has drawn much attention. Plenty of efforts were devoted to the development of renewable energies, such as the solar photovoltaic (PV) system. However, in a crowded country like Taiwan, it is difficult to find land for installing large scale solar farms. Due to this limitation, rooftop solar PV system is a space-efficient option to deploy renewable energies in the crowded urban area, and the government also encourage the general public to install solar PV system on their rooftops. In addition, it may also have the additional value of regulating urban temperature by altering the surface albedo. Although it can be an adaptive strategy for mitigating global warming, some studies show that the solar PV system can also have unintentional influence on the local climate as the number of solar panels increases. In particular, PV array deployment can change the surface radiative balance and thus enhance or reduce the urban heat island (UHI) effect. Therefore, if there are a lot of rooftop solar PV panels in the Taipei City, what is the impact on the local climate? Will the local temperature increase or decrease? How would it alter the local circulation and convection, and does that lead to changes in precipitation strength and spatial pattern?

1.1　Impact of Solar Photovoltaic Panel on Local Climate

There have been several studies discussing how solar PV panels would affect the global, regional, and local climate. Barron-Gafford et al. (2016) conducted an experiment in Arizona and monitored three different land covers nearby, wild desert, solar PV plants, and urban parking lot. They found that the monthly mean air temperature is the highest at the solar PV plants, even higher than the urban asphalt parking lot throughout the year.

1

This is a case of a photovoltaic heat island (PVHI) effect.

Scherba et al. (2011) used Energyplus building energy simulation software to model different kinds of sustainable roofing technologies, such as white roofs, green roofs, and solar PV panels in different cities; they found that when PV panels were added to white or green roofs, it would considerably increase the radiative heating and sensible heat flux to increase the temperature in the city; whereas temperature will decrease slightly for black roofs. In Taha (2013), mesoscale and meso-urban meteorological models, urbanized MM5 (uMM5), is used to evaluate the potential atmospheric impacts of solar panel deployment with the idea effective albedo (will be defined later). This study conducts a sensitivity test with different conversion efficiency ($10 \sim 30\%$) in the Los Angeles region. The simulations show no adverse impacts on air temperature and urban heat islands from largescale PV deployment; besides, when the solar conversion efficiency reaches 20%, some regional cooling can be noticed, and at the efficiency of 30%, the cooling effects reach up to 0.15 K. According to these studies, the impact of solar panels on climate may not always be the same but depends on the following two factors: the effective albedo of solar panels and the original background albedo.

Li et al. (2018) used the UMD–ICTP Earth System Model to simulate the installation of large-scale wind and solar farms in Sahara; they found that with a conversion efficiency of 15%, the temperature and the precipitation in the area would both increase. For solar farms, the reason may be the albedo effect and vegetation feedbacks. Because of the low conversion efficiency of PV panels, the effective albedo is lower than the original background albedo in Sahara, causing the surface to absorb more energy and increase temperature (maximal +1.28 K, minimal +0.97 K). The precipitation increase is because the warming effect in this area may cause a low pressure anomaly to induce moisture convergence. They also conducted different experiments with different conversion

2
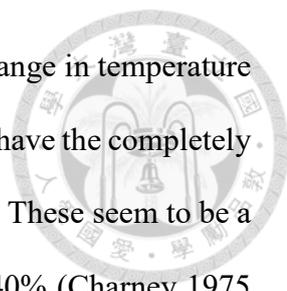
efficiencies and found that when the efficiency comes to 30%, the change in temperature and precipitation is very small; when the efficiency up to 45%, it may have the completely opposite result which cause cooling effect and precipitation decrease. These seem to be a straightforward result considering the background albedo of about 40% (Charney 1975 as cited in Li et al. 2018; Charney et al. 1977 as cited in Li et al. 2018).

The effective albedo is computed from the reflectivity and the conversion efficiency of solar panels. Because solar panels are expected to absorb as much solar energy as possible, the reflectivity would always be low. Therefore, the effective albedo highly depends on the conversion efficiency; the higher the conversion efficiency is, the higher the effective albedo would be. On the other hand, whether temperature and circulation may increase or decrease depends on the relationship between the effective albedo and the original background albedo. If the effective albedo is lower than the original background albedo, then there would be a warming effect, and the precipitation might increase. In contrast, if the effective albedo is higher than the original background albedo, then there would be a cooling effect, and might induce less precipitation in that area; if the difference of these two is small, then there would be no obvious influence to the climate.

3

1.2 Impact of Urban Heat Island on Afternoon Thunderstorm in Northern Taiwan

Taipei is located in a basin in northern Taiwan surrounded by the Linkou Tableland on the west, the Tatun volcano group on the north, and the Snow Mountain Range on the southeast (FIG. 1-1). Chen et al. (2007), Lin et al. (2011), and Kuo and Wu (2019) have shown that sea breeze along the Tamsui River and Keelung River valleys provide sufficient moisture and have convergence in the Taipei Basin. The confluent flow would extend southward to the Snow Mountain Range and acquire orographic lifting, which triggers deep convection and lead to heavy rainfall in the mountain area. In addition to the unique topography, Taipei is also the most crowded metropolitan area in Taiwan. They found that strong UHI effect would increase the accumulation and intensity of precipitation because cities become the warmer and create more unstable air masses; then the convection is enhanced to increase the rainfall downstream. Therefore, this study takes Taipei for a case study to investigate whether the citywide rooftop solar PV system would alter the local circulation and convection or not in response to an enhanced or reduced UHI effect.

The research objective of this study is to investigate whether there is some potential impact from the citywide solar PV system deployment or not. If the temperature increases after solar PV installation, it would enhance the UHI effect, and the accumulation or intensity of precipitation may increase, which might also lead to the probability of a flood increase; in this case, this consequence should be taken into consideration when the government promotes the solar PV system. On the other hand, if the temperature decreases, it would reduce the UHI effect, and the accumulation and intensity of precipitation may decrease, which might also lead to the probability of a flood decrease; then it can be another benefit and encouragement for the development of the solar PV

4

system which would reduce not only CO_2 emission but also the UHI and the probability of a flood. A meteorological model is applied to simulate how solar PV panels may affect the local climate and convective precipitation. The next chapter will describe how to deploy solar PV panels into the numerical model.
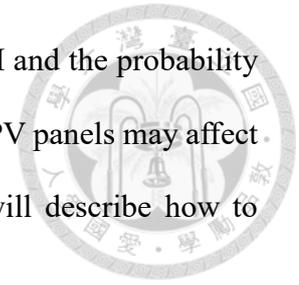
Chapter 2　　Data and Methodology

2.1　　Solar PV Panel Characteristics

According to Taha (2013), the influence of solar PV panels can be presented with the factor called effective albedo (α_e), which is computed as the following:

$$\alpha_e = \alpha + \eta \tag{1}$$

where α and η are respectively the reflectivity and energy conversion efficiency of the solar PV panels.

For the reflectivity, α, Taha (2013) provided typical values range from 0.06 to 0.1. In Masson et al. (2014), the reflectivity ranged from 0.11 to 0.16. The observation from the Department of Atmospheric Sciences in National Taiwan University shows that the reflectivity of the PV panels is about 0.12, which is a reasonable value compared to the above studies. Therefore, 0.12 is used for the reflectivity in this study. Some studies show that reflectivity of PV panels would change with the incident angle; when the incident angle is larger than 70°, the reflectivity would increase rapidly (Parretta et al., 1999; Balenzategui and Chenlo, 2005). However, when the incident angle is large, the effect of heat would be small in general. So, this study simply used a fixed reflectivity, and the influence from the changing reflectivity might need further investigated in the future.

The conversion efficiency η is defined as the following:

$$\eta = \frac{P_{max}}{E \cdot A} \tag{2}$$

where P_{max} is the maximum output power point of the PV panels; E is the input light irradiance (in W m^{-2}) under standard test conditions and A is the surface area of the PV panels (in m^2) (Meral and Dincer, 2011). In other words, the conversion efficiency η is the ratio of the PV output power to the solar input power. For this study, the top 50 power

6
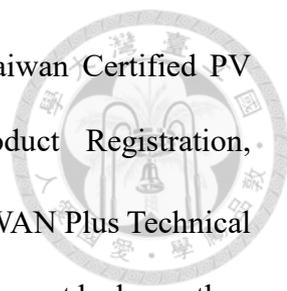
output of the PV modules are selected from the product list of Taiwan Certified PV Module (太 陽 光 電 模 組 產 品 登 錄 - PV Module Product Registration, https://www.tcpv.org.tw/Product/). In addition, according to PV TAIWAN Plus Technical Specification (2019), the decay of the conversion efficiency with time must be lower than 20% in 25 years. Therefore, if time decay is taken into consideration and assuming the worst situation that it would indeed drop by 20%, the conversion efficiency (considering time decay) $\eta = 17.63\%$ is used here (FIG. 2-1). Note that it is assumed that the time decay is linear, $\eta = \eta_0 \frac{1+(1-20\%)}{2} = 0.9 \cdot \eta_0$, where η_0 represents the original conversion efficiency of PV panels. Therefore, the effective albedo for the current conversion efficiency would be $0.12 + 0.1763 = 0.2963$ in this study.

FIG. 2-2 is an illustration of surface energy balance and the factors determining the effective albedo α_e. When the solar radiation S (the input power) reaches the surface of the PV panels, $(\alpha \cdot S)$ would be reflected where α is the albedo; whereas $(\eta \cdot S)$ would be converted into electricity. The portions $(\alpha \cdot S)$ and $(\eta \cdot S)$ are not absorbed by the PV panels; in other words, the effective albedo α_e represents the energy ratio that is not absorbed by PV panels; whereas the remaining portion, $(1 - \alpha_e) \cdot S$, would be absorbed and eventually convert into heat.

2.2 Rooftops and Land Use

In order to evaluate the effect of rooftop solar PV system in the Taipei City, the characteristics of solar panels discussed in the previous section need to be determined first, and then the area of rooftop available for PV installation needs to be estimated. The CTCI land use data (FIG. 2-3), which is converted from the 1/25,000 basic topographic map published by Ministry of the Interior (Tai et al. 2008), is used for the WRF model simulation. However, its resolution (about 1km × 1km) is too low for estimating the urban

7

area in the Taipei City. Thus, to define the urban area in the Taipei City precisely, the land use land cover data called GlobeLand30 (Chen et al. 2015) is used. GlobeLand30 is developed by the National High Technology Research and Development Program of China (863 Program) launched by the Ministry of Science and Technology of China named "remote sensing mapping and research on key technologies of global land cover" in 2010. The dataset covers land area from 80°N to 80°S, and consists of 10 land cover types with 30 m spatial resolution.

To figure out the coverage of rooftops, the 3D building data for the Taipei City is used. There are two sources for the building data; one is from the GitHub data set (台北市 3D 建築物, https://github.com/sheethub/tpe3d) which is retrieved from the government open data, Taipei City 3D Building Data (臺北市自動化 3D 近似建物模型, http://3d.taipei/tcg/kml/Taipei3DBuilding/Taipei3DBuilding.kml), established by Department of Information Technology, Taipei City Government. The other is from the Open Street Map project, which is a knowledge collective that provides user-generated street maps including 3D building data (Haklay and Weber 2008). FIG. 2-4 shows the land-use data from GlobeLand30 and the 3D building data. However, there are still some missing data in each data source. Therefore, this study sampled several regions with less missing building data to estimate the ratio of the rooftops to sampled area so that this ratio can represent the condition for whole Taipei City; the pink area represents the sampled regions in FIG. 2-4. The average rooftops ratio obtained from the sampled regions is about 0.52, and this value is assumed to be the same for the whole Taipei City. After the rooftop ratio is estimated, the GlobeLand30 land use data around the Taipei City is remapped back into the original CTCI land use data for WRF simulation. FIG. 2-5 shows the land use data after remapping by GlobeLand30.
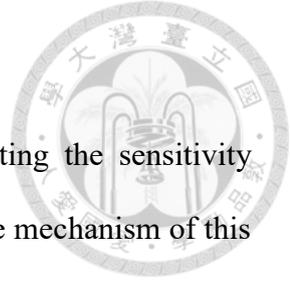
2.3 Case Overview

In this study, the 14 June 2015 case is selected for conducting the sensitivity experiments. Some studies have discussed the rainfall pattern and the mechanism of this strong afternoon thunderstorm case on 14 June 2015 (Jou et al. 2016; Miao and Yang 2020). Under a weak synoptic-scale forcing, the low-level convergence between sea breeze and the outflow induced by the rainfall at the mountainside causes deep convection in the Taipei Basin. FIG. 2-6 shows the surface analysis map from CWB at 0000 and 0600 UTC on 14 June 2015; there is no synoptic-scale weather systems near Taiwan. The 1-day accumulated rainfall from CWB is shown in FIG. 2-7, and the largest rainfall occurred on the south edge of the Taipei City.

2.4 The Numerical Model Experiment

2.4.1 The Model Setting

The high-resolution Weather Research and Forecasting (WRF) Model version 3.6.1 is used in this study. In order to improve the description of lower boundary conditions in urban area so that the impact of the urban rooftop PV installation can be simulated well, the Noah land surface model (Noah-LSM) and the Urban Canopy Model (UCM) selected as the physical options in the WRF model. The Noah-LSM model provides surface sensible and latent heat fluxes and surface skin temperature in the lower boundary. The UCM is a single layer model developed by Kusaka et al. (2001) and Kusaka and Kimura (2004). It simplifies the urban geometry into 2-dimensional infinitely-long symmetrical street canyons and provides better physical processes involved in the exchange of heat, momentum, and water vapor in urban environment. The following features relevant to this study are considered in the UCM: shadowing from buildings, reflection of short and longwave radiation, wind profile in the canopy layer and multi-layer heat transfer

9

equation for roof, wall and road surfaces.

FIG. 2-8 shows the simulation domain in this study. Three nest domains were constructed with spatial grid resolutions of 25 km, 5 km, 1 km, which respectively contained 100 × 107, 151 × 146, and 151 × 111 grid points. Other physical parameterization schemes applied in this study include the Morrison 2-moments scheme for microphysics, RRTM scheme for longwave radiation, Dudhia scheme for short wave radiation, Revised MM5 Monin-Obukhov scheme for surface-layer, MYNN 2.5 level TKE scheme for boundary-layer, Kain-Fritsch (new Eta) scheme for cumulus only for domain 1. The model run is set from 0600 UTC (1400 LST) and the total running period is 30 hours until the next day 12 UTC (2000 LST) for each experiment.

2.4.2 The Experiment Design

According to Kusaka et al. (2001) and Chen et al. (2004), the Noah LSM and the UCM coupling is realized by the parameter "urban fraction" which represent sub-grid scale (see FIG. 2-9 for the illustration of a model grid). The UCM estimates the surface flux and temperature for artificial surfaces, and the Noah LSM provides the other part for vegetated urban areas. Therefore, total surface fluxes for an urban grid can be written as

$$F_{total} = A_{natural} \times F_{LSM} + A_{artificial} \times F_{UCM} \qquad (3)$$

$$F_{total} = (1 - U_f) \times F_{LSM} + U_f \times F_{UCM} \qquad (4)$$

where F_{total} is the total surface flux including sensible and latent heat fluxes; $A_{artificial}$ is the area weighting of an artificial surface such as buildings and roads, and this also represents the urban fraction (U_f); $A_{natural}$ is the area weighting of a natural surface such as park and tree, and this can also be written as $(1 - U_f)$; F_{LSM} and F_{UCM} are the surface fluxes from the Noah LSM and the UCM respectively. In addition, the UCM estimates the surface flux for the rooftops, roads and walls separately, so F_{UCM} can be

separated into three components -- rooftops, roads and walls expressed as the following:

$$F_{UCM} = w_{rooftops} \times F_{rooftops} + w_{roads} \times F_{roads\ \&\ walls} \tag{5}$$

where $w_{rooftops}$ and w_{roads} are the area ratio of rooftops and roads, and $F_{rooftops}$ and $F_{roads\ \&\ walls}$ are the surface flux for rooftops, and roads and walls. Therefore, the total surface flux F_{total} would be

$$F_{total} = (1 - U_f) \times F_{LSM} + U_f \times (w_{rooftops}F_{rooftops} + w_{roads}F_{roads\ \&\ walls}) \tag{6}$$

To investigate the potential impact of rooftop PV installation, the rooftop albedo $\alpha_{rooftops}$ is replaced with the effective albedo α_e of PV panels, which would directly change the surface energy balance of rooftops. Therefore, the UCM would directly calculate the new surface fluxes for the rooftops and compute the new fluxes for the total grid by area weighting as the following:

$$F_{total} = (1 - U_f) \times F_{LSM} + U_f \times (w_{rooftops}F_{PV} + w_{roads}F_{roads\ \&\ walls}) \tag{7}$$

where F_{PV} is the new surface fluxes for the rooftops with PV installation.

Sensitivity experiments with different PV conversion efficiency were conducted. The first one is the control run (CRL) with the original rooftops albedo 0.15 (Lu, 2011) representing the original condition without solar panels. The second experiment is the scenario with the current technology, with a conversion efficiency of 17.63% (EF17) and the effective albedo is 0.2963. The last one is a future scenario; if our technology is improved and the conversion efficiency can reach up to 30% (EF30) which is expected to reach in the near future (Nemet, 2009) and its effective albedo is 0.42; the citywide PV installation would be deployed in the Taipei City (shown in FIG. 2-10).Basic assumptions made in these experiments include: without the consideration of the tilt angle of PV panels (Yang and Lu, 2007 and Benghanem, 2011 showed that there would be optimum tilt angles and orientation for PV installation) and the change of PV panels' reflectivity with incident angle.

Chapter 3   Results

3.1   The Control Run

In this chapter, the afternoon thunderstorm case 14 June 2015 is chosen to demonstrate the impact of solar PV installation, and this paragraph would have a brief introduction for the CTL run. FIG. 3-1 shows the spatial distribution of 6-hr (1200 ~ 1800 LST) accumulated rainfall. Most of the intense precipitation occurred over the Snow Mountain Range. A secondary intense rainfall area occurred to the south of the Taipei City. The background wind field in FIG. 3-2 shows an overall southwesterly at 1400 LST. FIG. 3-3 shows the evolution of the winds and rainfall from 1000 to 1600 LST. Because of the sea breeze effect as well as a wake flow induced by the synoptic-scale southwesterly wind (the background winds) against the mountain ranges, the near surface onshore wind blows along the Tamsui River valley and Keelung River valley, which converged in the Taipei Basin (FIG. 3-3a, 3-3b). The southward confluent flow further extends to the Snow Mountain Range and acquires orographic lifting, which triggers deep convection and causes heavy rainfall in the mountain area (FIG. 3-3c, 3-3d). Heavy precipitation also occurs to the south of Taipei City in FIG. 3-3e. Therefore, later discussions on the rainfall pattern can be simply divided into two parts, deep convection in the mountains and the heavy rainfall near the Taipei City.

3.2   Impact after PV Installation

3.2.1   Temperature

In the experiments of the solar PV deployment, the temperature change may be the most intuitive impact due to changes in the surface energy balance. FIG. 3-4 shows the
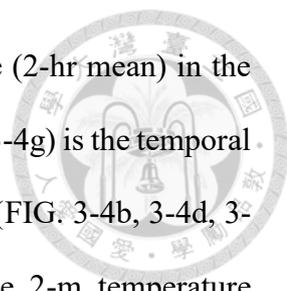
differences (compared with the CTL run) in the 2-m air temperature (2-hr mean) in the two PV installation runs. The left column (FIG. 3-4a, 3-4c, 3-4e, and 3-4g) is the temporal evolution of the EF17 run from 1000 ~ 1200 LST; the right column (FIG. 3-4b, 3-4d, 3-4f, and 3-4h) is for the EF30 run. The spatial distribution of the 2-m temperature difference can be roughly explained by the short wave radiation (SW) absorption (FIG. 3-5 and FIG. 3-6) and the sensible heat flux (SH) (FIG. 3-7) at the surface. These two have similar patterns because the more SW surfaces absorb the more SH surfaces can release (latent heat flux LH is small in the urban area). The 2-m temperature decreases in both runs in the urban area before 1400 LST. Temperatures in the later afternoon are strongly influenced by cloud cover and thus not discussed. Because the solar PV effect is represented by the effective albedo, less SW is absorbed to the surface in the Taipei City, which results in less SH and a cold island effect (CIE); the EF30 run has stronger CIE (maximum about 0.5 °C) than the EF17 run (maximum about 0.25 °C) as expected because the EF30 run has higher effective albedo 0.42 than the EF17 run 0.2963 (both higher than the CTL run 0.15).

There is a wide area of warming near Taoyuan before 1200 LST, which is not a direct effect of the PV panels. This phenomenon can also be explained by the absorbed SW and SH. FIG. 3-5 shows that there is an area of relatively high SW absorption moving from the northern coastline to the Snow Mountain Range. In the CTL run, there is a cloud band passing by, which may block the sunlight. The relatively high SW absorption area in FIG. 3-5 should be a result of decreased coverage or cloud thickness of the cloud band in the PV deployment runs. However, strong warming also happened in 1400 ~ 1600 LST near the Taipei City in the both EF17 and EF30 runs (FIG. 3-4g and 3-4h). This would be the consequence that the cloud cover changed in association with the weakened convection in the Taipei City, so that there are fewer clouds near the Taipei City and the surface can

absorb more SW than the CTL run (FIG. 3-6c and 3-6d). This will be further discussed in Chapter 3.2.3.

3.2.2　Wind

The temperature changes will also have impact on the local circulation. FIG. 3-8 shows the 2-hr mean wind difference in 1000 ~ 1200 LST; the vectors represent the wind difference and the shading is wind speed difference. There are some strong signals offshore to the north; this might be some accumulated effect from the previous day simulation, which will be discussed in Chapter 4.1. Both EF17 and EF30 runs exhibit similar patterns on land. Along the Tamsui River valley, there is a westward wind difference against the onshore wind to the west of the Taipei City till the coastline. On the other hand, the onshore winds from the Keelung River valley become stronger. To the south of the Taipei City, the southward wind that blows against the Snow Mountain Range are enhanced in both EF17 and EF30 runs; thus, the onshore winds can further extend to the mountain range.

To further investigate the winds that blow toward the foothills, a comparison of the N–S vertical cross section after a 10–km horizontal average (the red N–S box in the FIG. 3-8b) is shown in FIG. 3-9 (1000 ~ 1100 LST) and FIG. 3-10 (1130 ~ 1230 LST). The temporal evolution exhibits a potential temperature gradient (contour) between the Taipei City and the mountain area. FIG. 3-9 and FIG. 3-10 show that the minimum potential temperature at the basin (lower-right region of each figure) is smaller in the EF17 and EF30 runs compared to the CTL run, which indicates that a larger potential temperature gradient occurs after the PV deployment. The larger potential temperature gradient would cause a larger pressure gradient which strengthens the onshore winds so that the stronger upslope flow happens in the mountain area (the darker shading is shown in the EF17 and EF30 runs), and the EF30 run has the largest potential temperature gradient and the

strongest upslope flow.

3.2.3 Precipitation

The results of the precipitation change after the PV deployment are shown in FIG. 3-11 and FIG. 3-12. The pattern of differences in precipitation is not uniform, with areas of rainfall increase and decrease alternately ordered. The rainfall-decrease regions are often associated the upslope position, which may imply that those rainfall regions shifted upslope (usually southward) toward the mountains. From the temporal evolution of rainfall in FIG. 3-12, there is a strong rainfall decrease at the southern edge of the Taipei City in 1400 ~ 1600 LST along with a strong rainfall increase at the mountainside southwest of it. The former may be directly influenced by rooftop PV panels in the urban area, while the latter is remotely influenced by the change in dynamics that associated with the changes in the Taipei City.

To have a better understanding of this precipitation change pattern, FIG. 3-13 and FIG. 3-14 show the NE–SW vertical cross section of the vertical velocity and the radar reflectivity along the background wind flow (southwesterly, FIG. 3-2) after a 10–km horizontal average (the red NE–SW box in the FIG. 3-11c) during 1400 ~ 1500 LST. In FIG. 3-13a, 3-13d and 3-13g, deep convection (called the convection A) occurred at the foothill (24.94°N < x < 25.01°N) in all three runs at 1400 LST. However, there is another convection region (called the convection B) at the mountainside in the EF17 and EF30 runs, which may result from the stronger upslope flow for orographic lifting. Then, in FIG. 3-13b, 3-13e and 3-13h, these convective systems propagate downstream following the high-level southwesterly and reach the Taipei basin. Convection A arrived the Taipei City (x > 25.01°N, the black box) in the CTL run at 1430 LST, in the EF17 run with a weakened strength compared to the CTL run. In the EF30 run, the convection A has not

reached the Taipei City (x > 25.01°N, the black box) at 1430 LST yet, but the convective strength is still strong. Convection B moved downslope with the background southwesterly in the EF17 and EF30 runs, while it just appeared not until 1430 LST in the CTL run. At 1500 LST, convection A weakened a lot in the CTL run and almost disappeared in the EF17 and EF30 runs (FIG. 3-13c, 3-13f and 3-13i). Convection B moved further downslope to the foothill, and its outflow associated with rainfall seems to induce another convective system upslope.

FIG. 3-14 shows the vertical cross section of the radar reflectivity. The CTL run has the strongest rainfall signal from convection A at 1400 LST. The EF30 run shows the weakest signal from convection A but the strongest signal from convection B. By comparing with the results in FIG. 3-13, it is found that the region with strong upward vertical motion is separated from the strong rainfall region and locates downstream of convection A in all runs, which indicates a propagation of the convective system. At 1430 LST, the region with strong upward vertical motion is still separated from the heavy rainfall region for convection A in the CTL run, but these two regions become overlapped in the EF17 and EF30 run. Such overlapping may weaken the deep convection because of the precipitation downdraft may suppress updraft if they are aligned.

Therefore, the precipitation change during 1400 ~ 1600 LST in the red box region in FIG. 3-11c can be separated into two parts. Firstly, the convection at the mountainside occurred earlier at 1400 LST than the CTL run at 1430 LST, which causes the precipitation increase at the upstream area. This may be explained by the upslope wind speeds which are larger in EF17 and EF30, so the convection in the mountain would develop stronger or at a higher slope. Secondly, the deep convection triggered from the foothill does not propagate into the Taipei City as the CTL run does. In the EF17 run, although the deep convection does move into the Taipei City, the intensity of the deep

convection decreased; in the EF30 run, the deep convection does not even get near the Taipei City. This may result from the CIE as the reduced near-surface temperature would lead to higher air density and thus reduced buoyancy to cause a more stable environment. The overall influence may look like a blocking effect for the propagation of the convective system moving toward the Taipei City.

Chapter 4　Discussion

4.1　Other Cases

In addition to the 14 June 2015 case, other afternoon thunderstorm events were also tested in this study, including the events on 23 June 2015, 17 June 2016, and 10 June 2017. Both the 23 July 2015 and 17 June 2016 cases had intense rainfall with southwesterly monsoon influence, although there was a stationary front a little bit close to the northern coast for the latter one. The 10 June 2017 case was also under the influence of southwesterly monsoon, but only light rainfall was produced; therefore, the rainfall difference signal is weaker than the other cases in the following results. FIG. 4-1 and FIG. 4-2 show the 6-hr accumulated rainfall in the CTL run, and the 6-hr accumulated rainfall difference between the EF17/EF30 run and the CTL run. All three cases have a similar pattern in rainfall differences. Because of the background southwesterly, most of the precipitation occurred over the Snow Mountain Range. There is a rainfall decrease region near the southern edge of the Taipei City, and surrounded by the rainfall increase regions, which may imply that the precipitation regions shift toward the mountain area. These results are also consistent with the findings for the case discussed in Chapter 3, suggesting that the rooftop solar PV .effect on precipitation around Taipei is robust.

4.2　Uncertainties

There are several uncertainties in the above estimations. Firstly, the simplified parameterization of solar PV panel characteristics is applied for the simulation. The idea of the effective albedo regards the solar PV panels as a high-albedo material so that the overall influence from the PV system is converted into the reflected SW, and this design
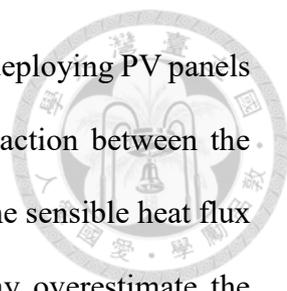
is actually closer to replacing the rooftops with PV panels instead of deploying PV panels that are not fully in contact with the rooftops. Therefore, the interaction between the rooftops and the PV panels is ignored, such as the SW, the LW and the sensible heat flux between the solar PV system and the rooftops. This treatment may overestimate the strength of CIE because the PV panels would capture the reflected SW by the surrounding and the upward LW from the rooftops below. Other assumptions used in this study include a fixed tilting angle for PV panels and temperature-independent conversion efficiency (the conversion efficiency actually decreases as the temperature of the PV panel rises).

Secondly, the single layer urban canopy model (UCM) might not be the best option available. There are some multi-layer urban canopy model schemes in the WRF model. The building effect parameterization (BEP; Martilli et al. 2002) considers the vertical distribution of buildings for the sources and sinks of heat, moisture and momentum through the whole urban canopy layer. Although UCM also uses the standard deviation to consider the distribution of the building height, it may not fit well the real building height distribution for everywhere. BEM (Salamanca and Martilli, 2010), a simple building energy model, additionally considers the energy exchange between indoors and outdoors. Therefore, the urban canopy model scheme BEP + BEM may be closer to the reality. Moreover, the rooftop ratio is estimated by the 3D building data, but there is some missing data in both data sources. Therefore, the assumption is made that the rooftop ratio for each grid is represented by the average rooftop ratio of the sampled regions with less missing value, which would have different results with different sampled regions. Thus, a more complete 3D building data set is needed to evaluate more realistic rooftop ratios.

Thirdly, the total running period of the WRF model is 30-hr in this study. Although this is intended to acquire a longer spin up time to reduce initialization error, it may also produce accumulated effect from the previous day, which may muddy the signals seen in
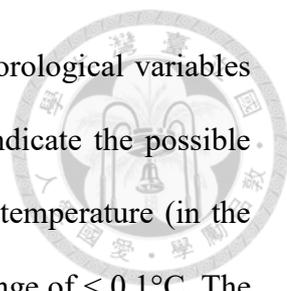
the next day can cause problem in result interpretation. Thus, meteorological variables before sunrise (0600 LST) on the analyzed day are compared to indicate the possible accumulation effect. The results show a slight decrease in the 2-m temperature (in the Taipei City in EF17 compared to the CTL run, with a maximum change of $< 0.1°C$. The maximum CIE in the sensitivity experiments reached $0.25°C$ and $0.5°C$ for the EF17 and EF30 runs, respectively, which are significantly higher than the "accumulation effect." For the 2-m water vapor mixing ratio, the EF17 and EF30 runs both have more water vapor in the Taipei City at 0600 LST while the rainfall accumulation for both runs are decreased in the Taipei City. Therefore, the accumulated effect does not alter the overall results but still has some influence such as the strong signal over ocean north of Taiwan that shown in FIG. 3-8. The difference in the absorbed SW in FIG. 3-5 may also be affected somewhat by the accumulated effect.

## 4.3   Cold Island Effect (CIE) Strength

According to the sensitivity experiments in this study, there exist a cold island effect (CIE) at the PV installation area in the Taipei City; the higher the conversion efficiency is, the stronger CIE is. Besides the conversion efficiency, the coverage range of the PV deployment is also another crucial aspect. One may suspect that a wider coverage should enlarge the range of the CIE. The scenario might occur if the New Taipei City or even whole Taiwan decided to exercise extensive rooftop PV installation. However, even with the same strength and range of the CIE, the consequence may be different in different locations due to the fact that temperature is not the only condition for the development of convective systems. The location of the maximum temperature gradient, the moisture and lifting mechanisms are also important, which are highly affected by the geographic layout.

4.4 Geographical Layout

Taiwan is a small island surrounded by sea with a complex geographic environment. The key geographic layout for summer convection in Taiwan is the short distance from the coastline, through the plain, and into the mountains. Studies have shown that the afternoon thunderstorms in Taiwan resulted from the interaction of the wake flow induced by the background winds, sea breeze, and upslope winds caused by the terrain (Chu 2019; Kuo and Wu, 2019; Miao and Yang 2020). Therefore, this layout, sea-plains-mountains, plays an important role for the afternoon thunderstorms in Taiwan. Any temperature change may alter the local circulation on land. For example, the urban heat island effect is the warming effect of the cities at the plains; it would increase the temperature gradient between the plain and the sea but decrease the potential temperature gradient between the plain and the mountains, so sea breezes would become stronger but anabatic winds may become weaker. However, the sea breezes are strong enough so that the overall upslope flow might not decease. By contrast, the CIE is a cooling effect over the plain area in this study, which would decrease the temperature gradient between the plain and the sea but increase the potential temperature gradient between the plain and the mountains. This means that the sea breezes would become weaker but the anabatic winds may become stronger. Therefore, the overall upslope flow still increases. The above analysis points out that the geographic setting of the city for rooftop PV installation is important to the effect on circulation and convection.

4.5   Geo-engineering

The previous discussion indicates that the solar PV panels can be used not only for renewable energy but also a means to regulate the near surface temperature, as well as to alter local circulation and cause precipitation change. This idea actually is similar to the concept of geo-engineering for mitigating adverse effects of global warming by large-scale intervention. The geo-engineering on a global scale is not discussed here because it is quite unpredictable and uncontrollable. But, if the impact of solar PV panels on a local scale can be well understood, there may be a chance for small scale (city scale or street scale) applications. Because of the policy and the encouragement from the government, the solar PV installation is getting more prevalent for the general public. Under this premise, it can be expected that more solar PV panels will be deployed in the near future. If there is a better knowledge of the subsequence after PV deployment, besides the use for CO_2 reduction, it may also provide a solution for other issues. For instance, this study shows that the PV installation in the Taipei City would reduce the UHI and also weaken the rainfall intensity near the Taipei City, which may provide another option to deal with flooding. Another example, to better the ventilation for a community or a city, increase the temperature gradient with the CIE from the PV system at specific locations, which would increase the near-surface wind speed. On the other hand, it should also be well investigated before the citywide PV deployment in case some unexpected side effect happens.
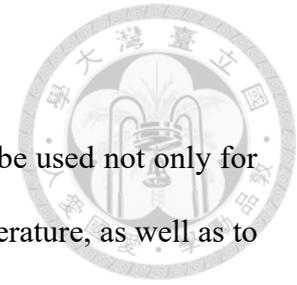
Chapter 5 Conclusion

In dealing with the global warming effect, people start to develop some mitigation and adjustment actions, such as the encouragement of renewable energy usage. Nevertheless, there are always consequences for every action. Take solar PV energy for an example; several studies have already started discussing about the potential influence on the environment, and have found that solar PV panels may change the near surface temperature (Scherba, 2011; Taha, 2013) because of the change in the surface energy balance. However, the temperature change may further induce other issues, such as circulation and precipitation. Therefore, this study tried to investigate how the solar PV installation changes the local circulation and convection in Taipei.

The numerical model WRF coupled with Noah-LSM and UCM is used to conduct sensitivity experiments with different PV energy conversion efficiencies. The results show that PV installations lead to a cold island effect (CIE) in the Taipei City. The decrease in near surface temperature over the urban area may change the temperature gradient between the urban area and the mountain slope at the south of the Taipei Basin, which may induce a stronger upslope flow to trigger an earlier convection at the higher levels over the mountain range. Later, the deep convection is triggered at the foothill and moves northeastward, toward the Taipei City. However, the CIE in the Taipei City provides a higher air density and a more stable environment, which would result in an overall blocking effect that prevents the deep convection from propagating into the Taipei City. The accumulated rainfall change pattern can be summarized in two parts, the upslope shifting for the rainfall regions in the mountain and the decrease in heavy precipitation on the southern border of the Taipei City. Both changes are more obvious when a future PV conversion efficiency of 30% is applied comparing to that with the

current PV conversion efficiency of 17.63%.

As mentioned in Chapter 4, some improvements can be made in this study, such as using a more sophisticated parameterization scheme for solar PV, use the more realistic multi-layer urban canopy model (BEP + BEM) for the urban scheme, try to eliminate the accumulated effect from model spin up by reducing the simulation time. Extensions of this study may include the investigation on coverage change by extending the solar PV installation area to the New Taipei City or other cities of Taiwan where enforcement of renewable energy policy are planned. With a better understanding of the impacts of solar PV system, there may also be some applications for mitigation strategies, such as the local-scale geo-engineering. By controlling the temperature change and the local circulation, solar PV is not merely a means of renewable energy but also provides a different aspect for regulating urban circulation and precipitation.
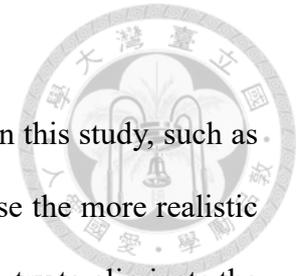
FIGURES

FIG. 1-1.   The topography of northern Taiwan (satellite images from Google Earth).
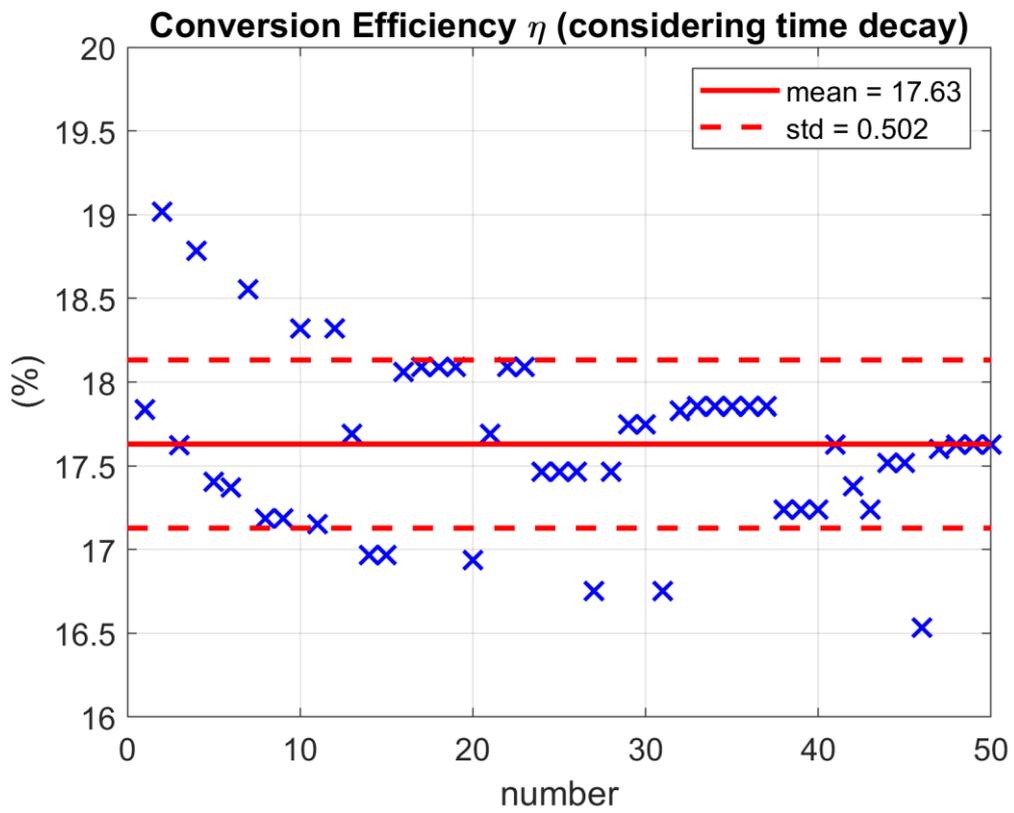
FIG. 2-1.　The scatter plot of the conversion efficiency from the top 50 power output PV modules from the product list of Taiwan Certified PV Module, TCPV Module (2019). The solid line is the mean of 50 conversion efficiency. The dot line is the standard deviation.
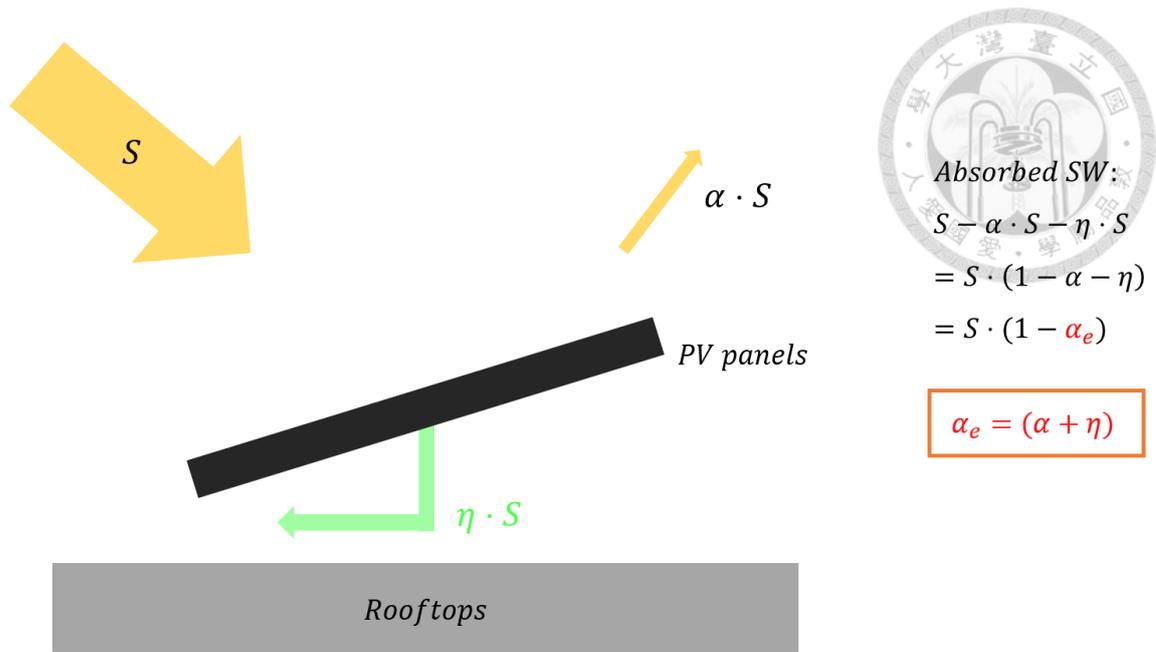
FIG. 2-2. Illustration of the effective albedo for the current conversion efficiency. S represents solar radiation; α is the albedo of PV panels; η is the conversion efficiency of PV panels; $α_e$ is effective albedo.
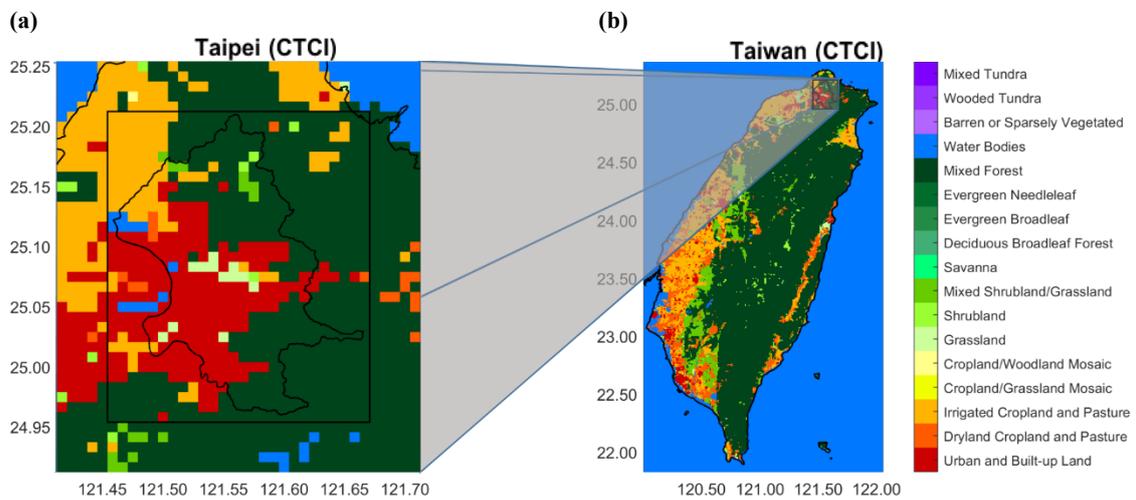
FIG. 2-3. The CTCI land use data in the WRF model. (a) Taipei is zoomed in from (b) Taiwan.

27
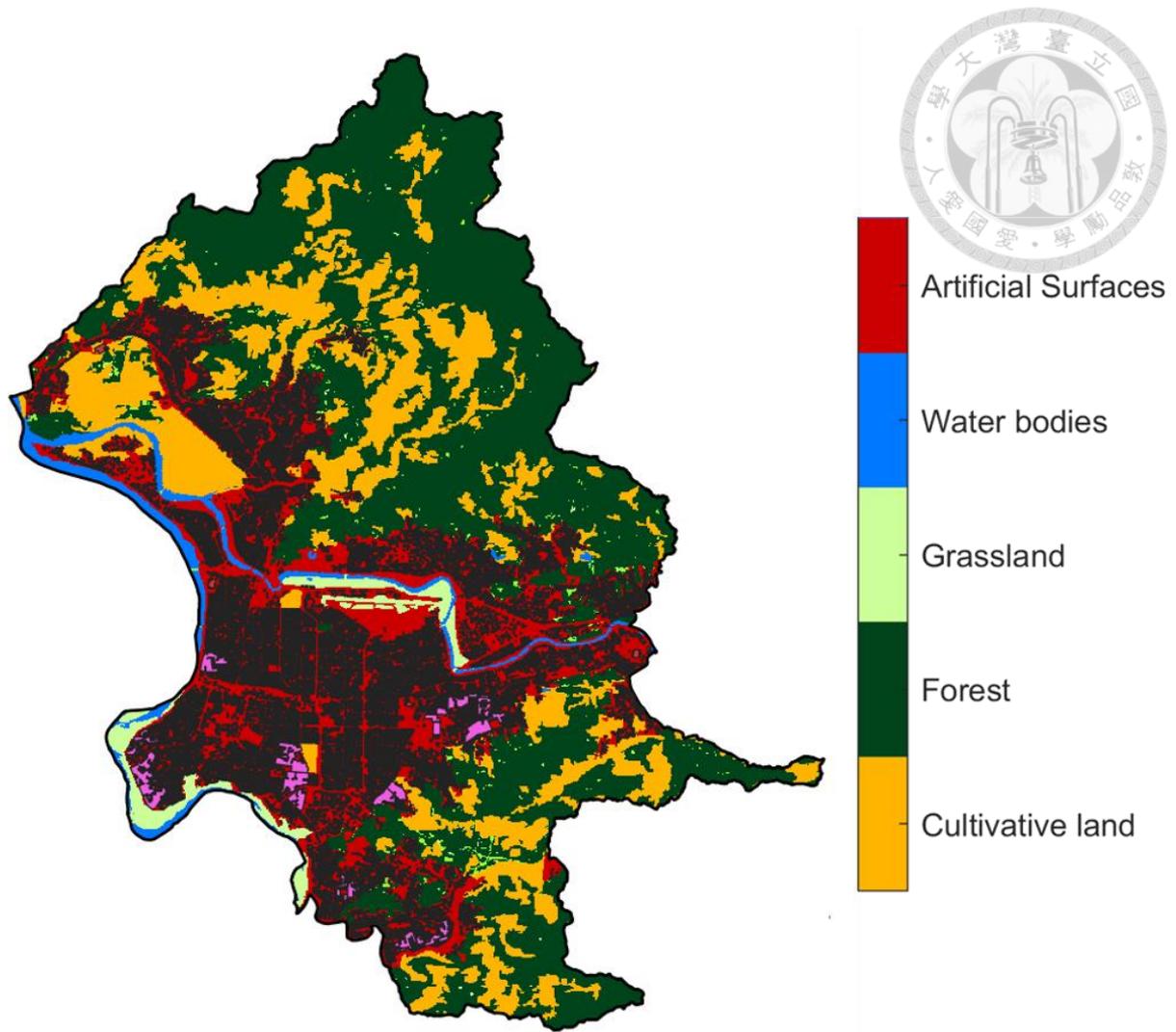
FIG. 2-4. The land use data of GlobeLand30 and the building data (black area) of the Taipei City. The pink area represents the sampled regions for rooftop ratio and the average is about 0.52
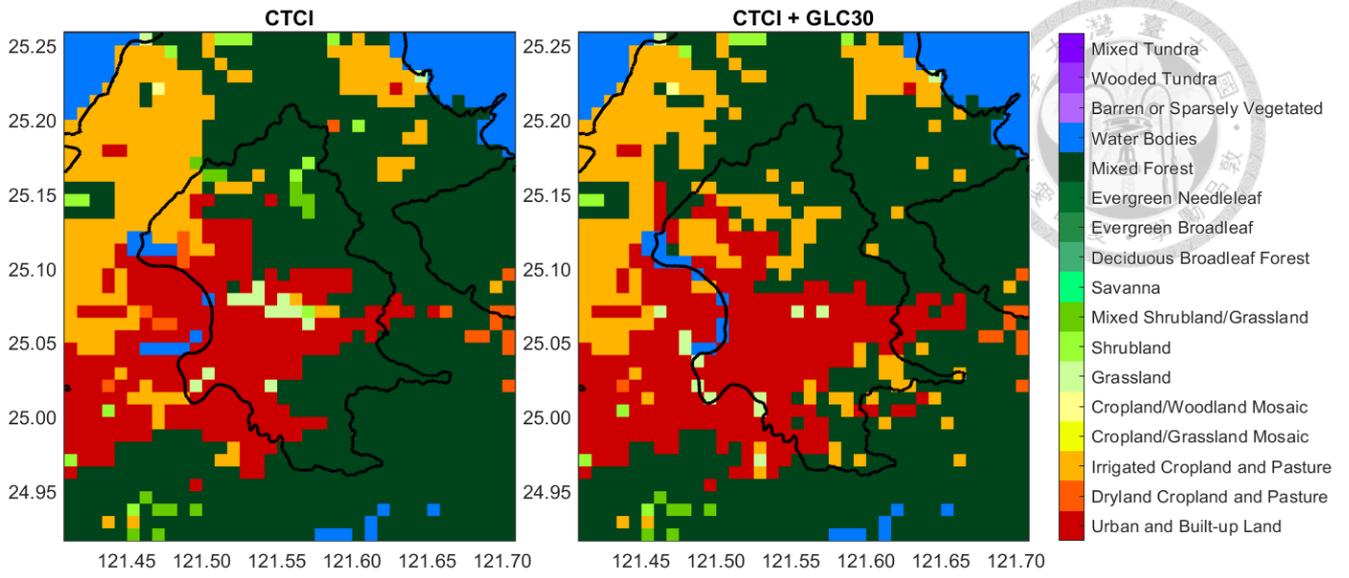
FIG. 2-5.   The land use data after remapping by GlobeLand30.
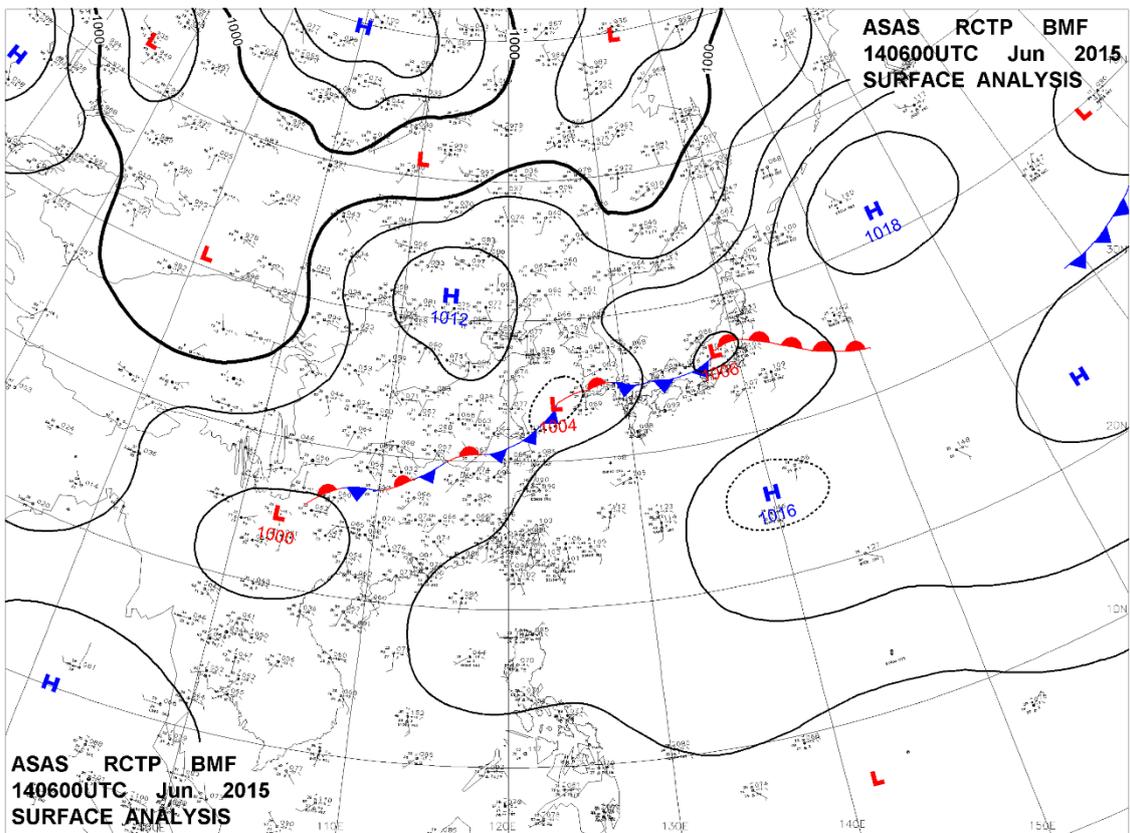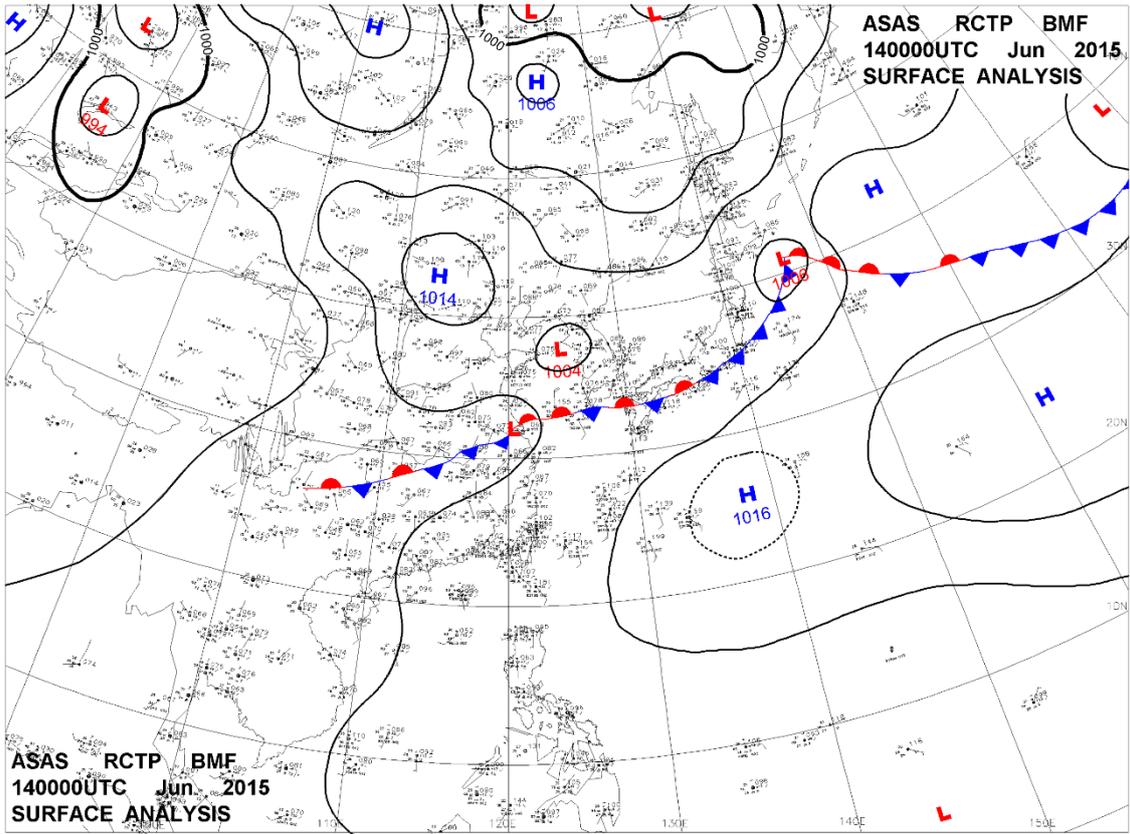
FIG. 2-6. The surface analysis map from CWB at 0000 and 0600 UTC on 14 June 2015.
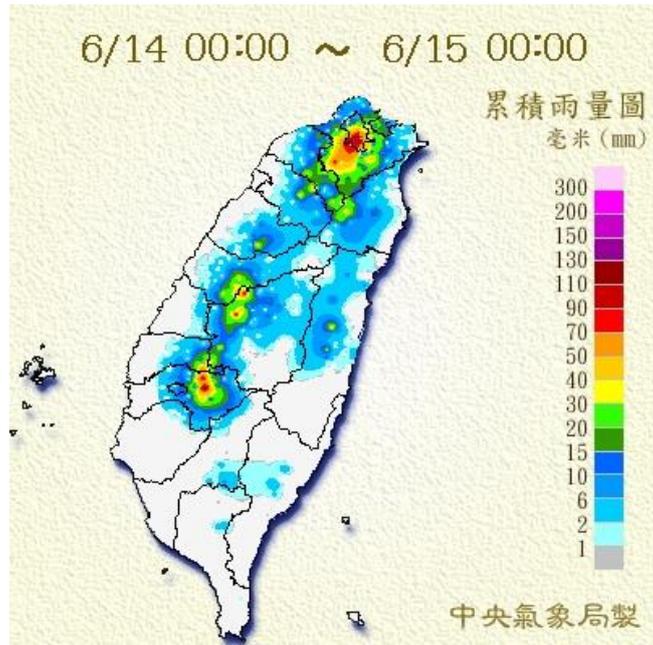
FIG. 2-7. The 1-day accumulated rainfall from CWB on 14 June 2015.

WPS Domain Configuration
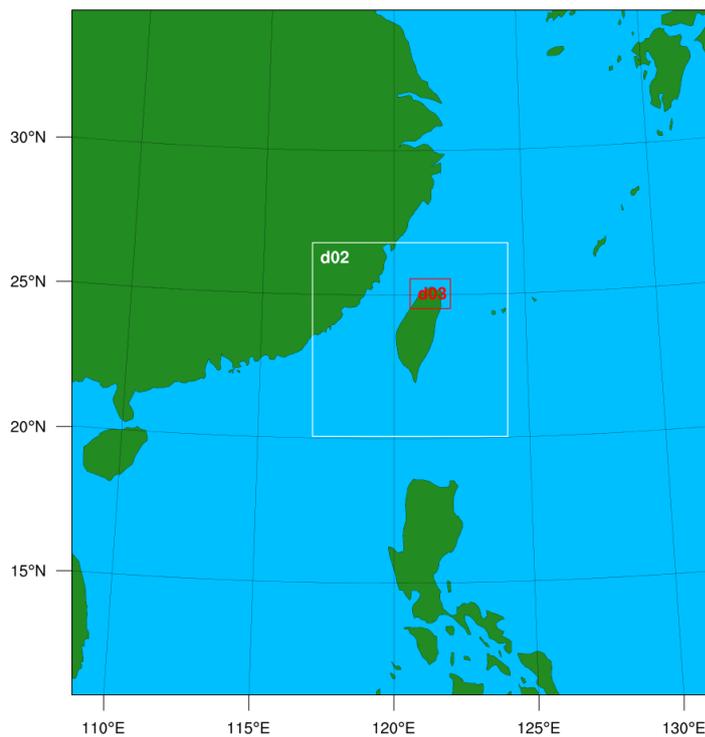
FIG. 2-8. Three nested domains (with the resolution 25 km, 5 km and 1 km respectively)

of the WRF model.

$$F_{total} = U_f(w_{rooftops} \cdot F_{rooftops} + w_{roads} \cdot F_{roads\,\&\,walls})$$
$$+ (1 - U_f) \cdot F_{natural}$$

$$F_{total} = U_f(w_{rooftops} \cdot F_{PV} + w_{roads} \cdot F_{roads\,\&\,walls})$$
$$+ (1 - U_f) \cdot F_{natural}$$
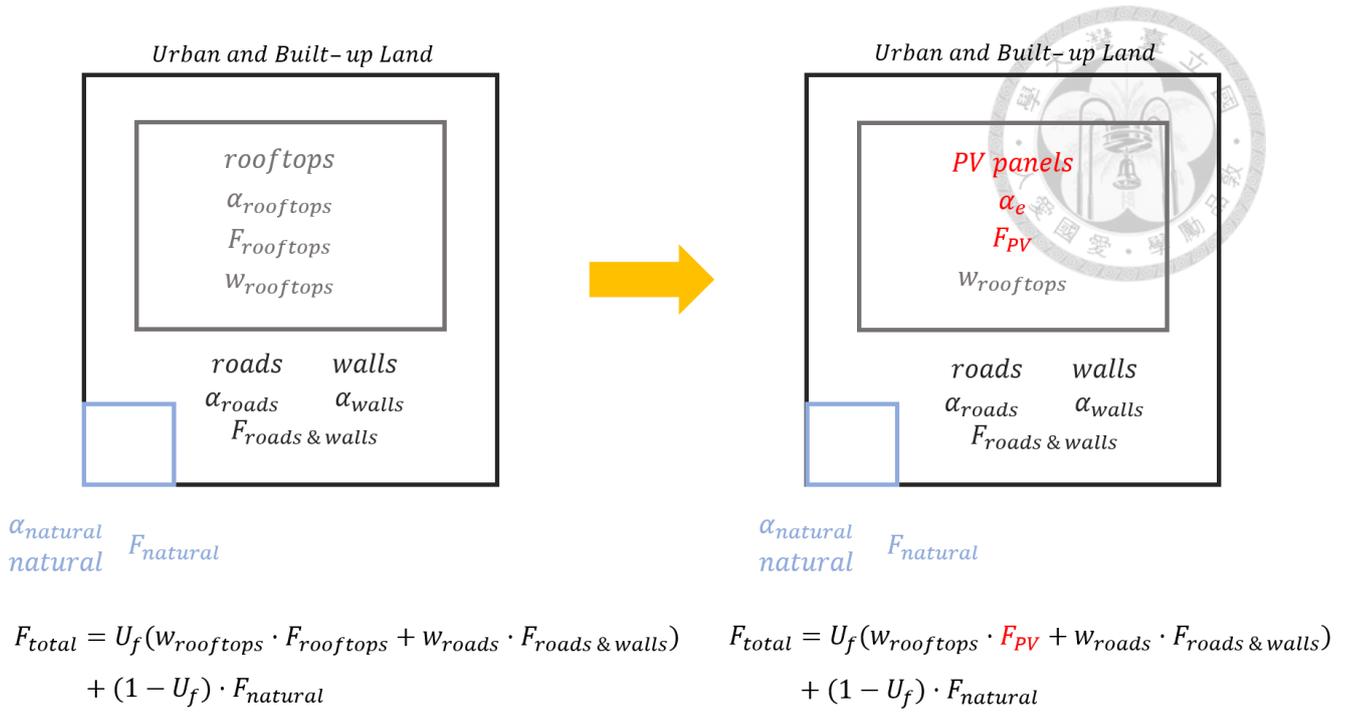
FIG. 2-9. The illustration of a grid. $\alpha_{rooftops}$, α_{walls}, α_{roads}, $\alpha_{natural}$ and α_e are respectively the albedo of rooftops, walls, roads, natural surface, and effective albedo of solar panels; $w_{rooftops}$ and w_{roads} are respectively the area weighting of rooftops and roads; U_f is the urban fraction and F_{total}, $F_{rooftops}$, $F_{road\,\&\,walls}$, and $F_{natural}$ are the surface flux from a total grid, rooftops, roads and walls, and natural surfaces.
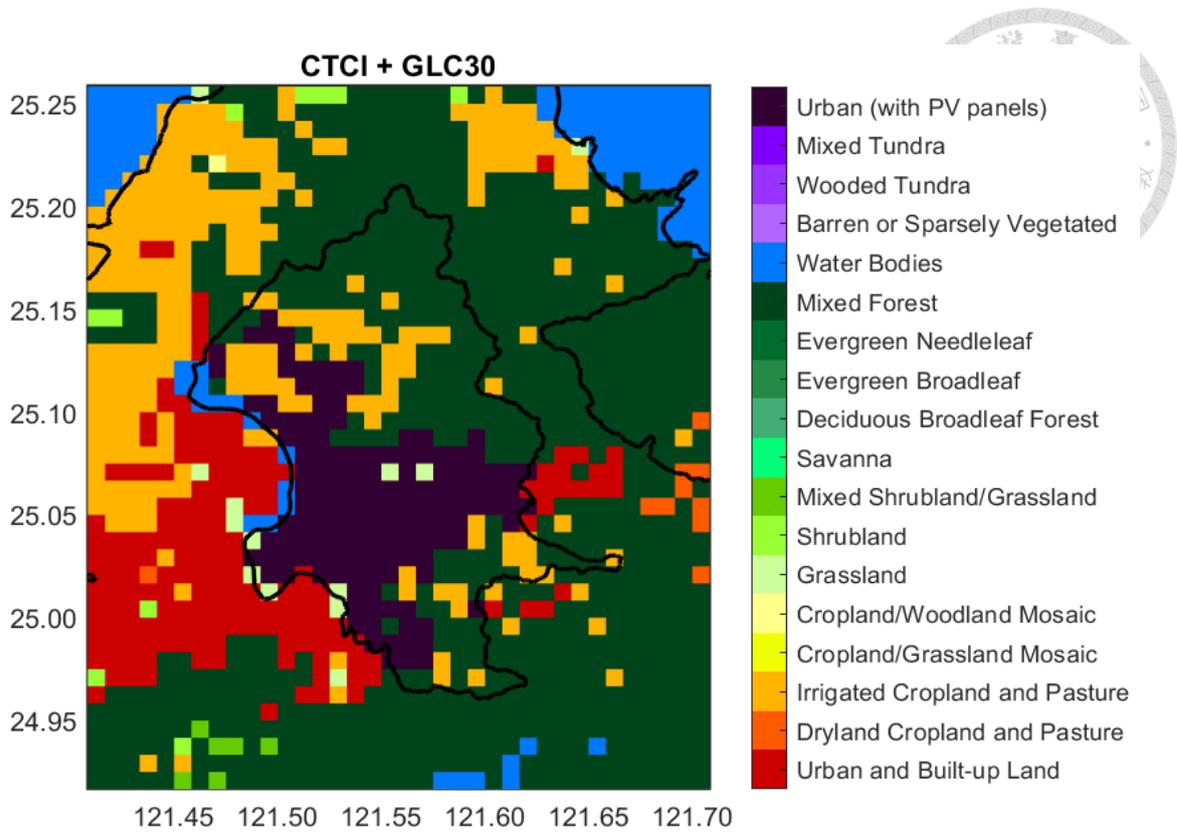
FIG. 2-10. The coverage of the PV installation (dark purple) in the whole Taipei City.
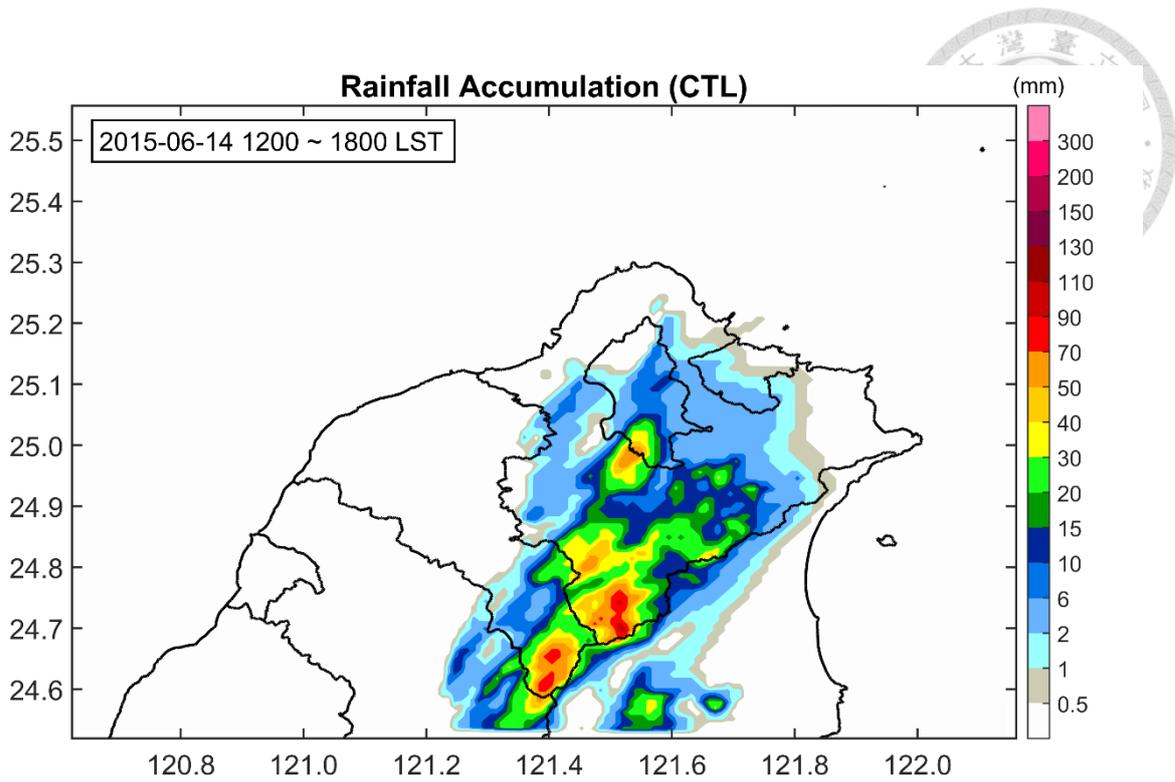
FIG. 3-1.   The 6-hr (1200 ~ 1800 LST) accumulated rainfall in the CTL run.
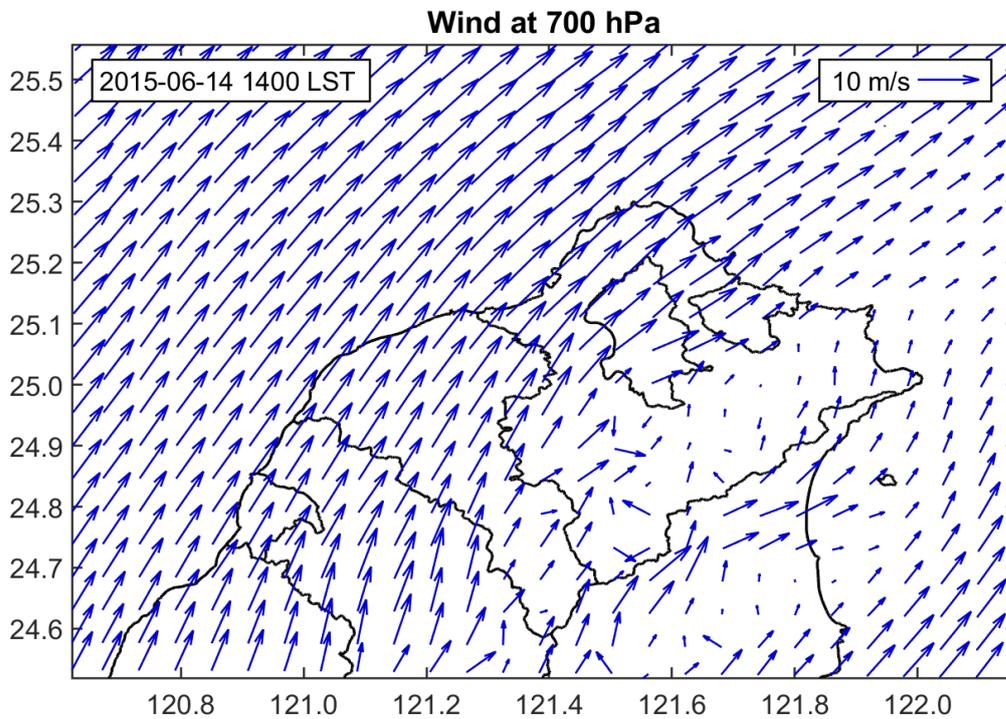
FIG. 3-2.   The winds at 700 hPa in the CTL run.
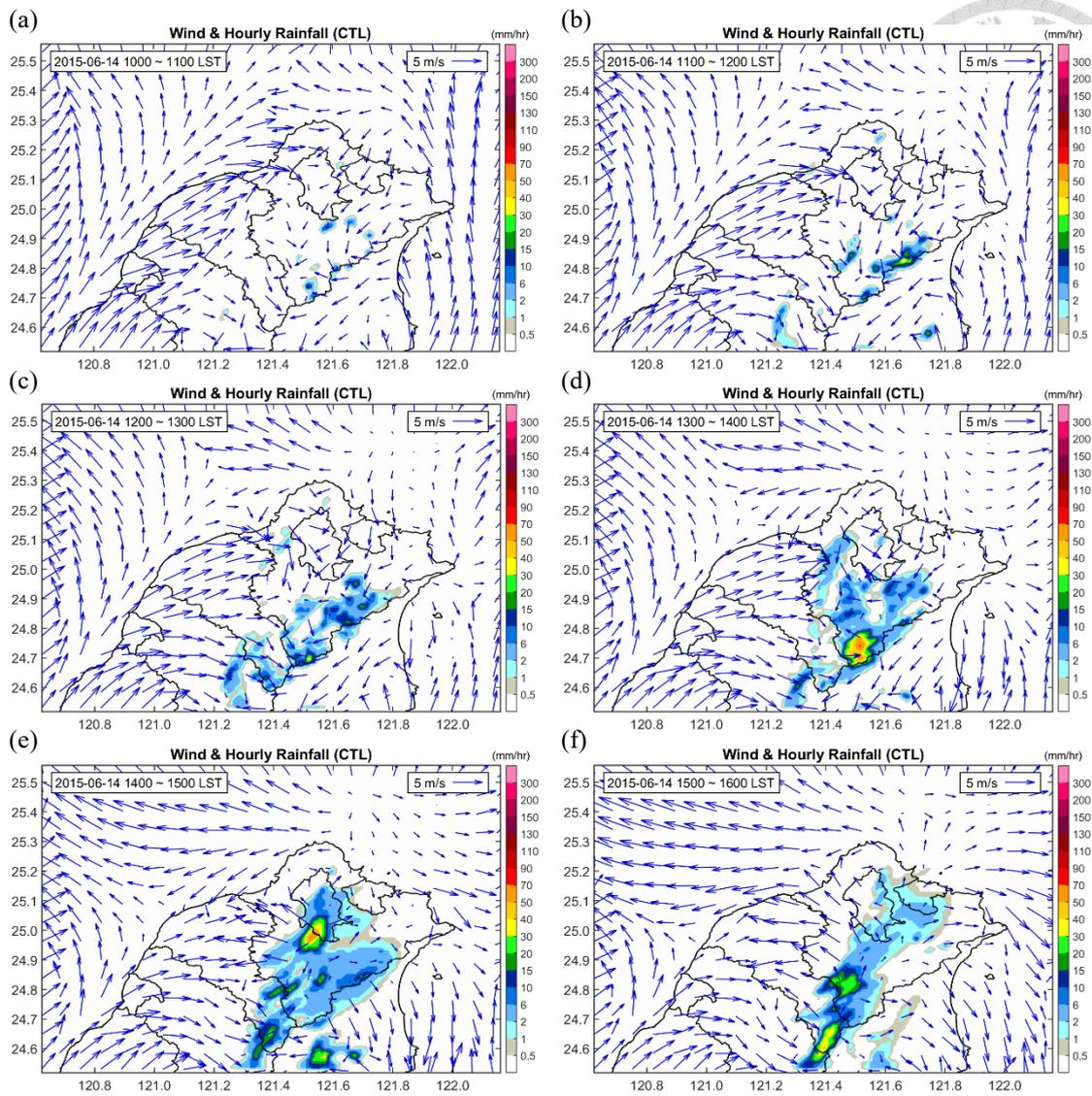
FIG. 3-3.   The time evolution from 1000 ~ 1600 LST in the CTL run, vectors for 10-m winds (near surface winds) and shading for the hourly rainfall.
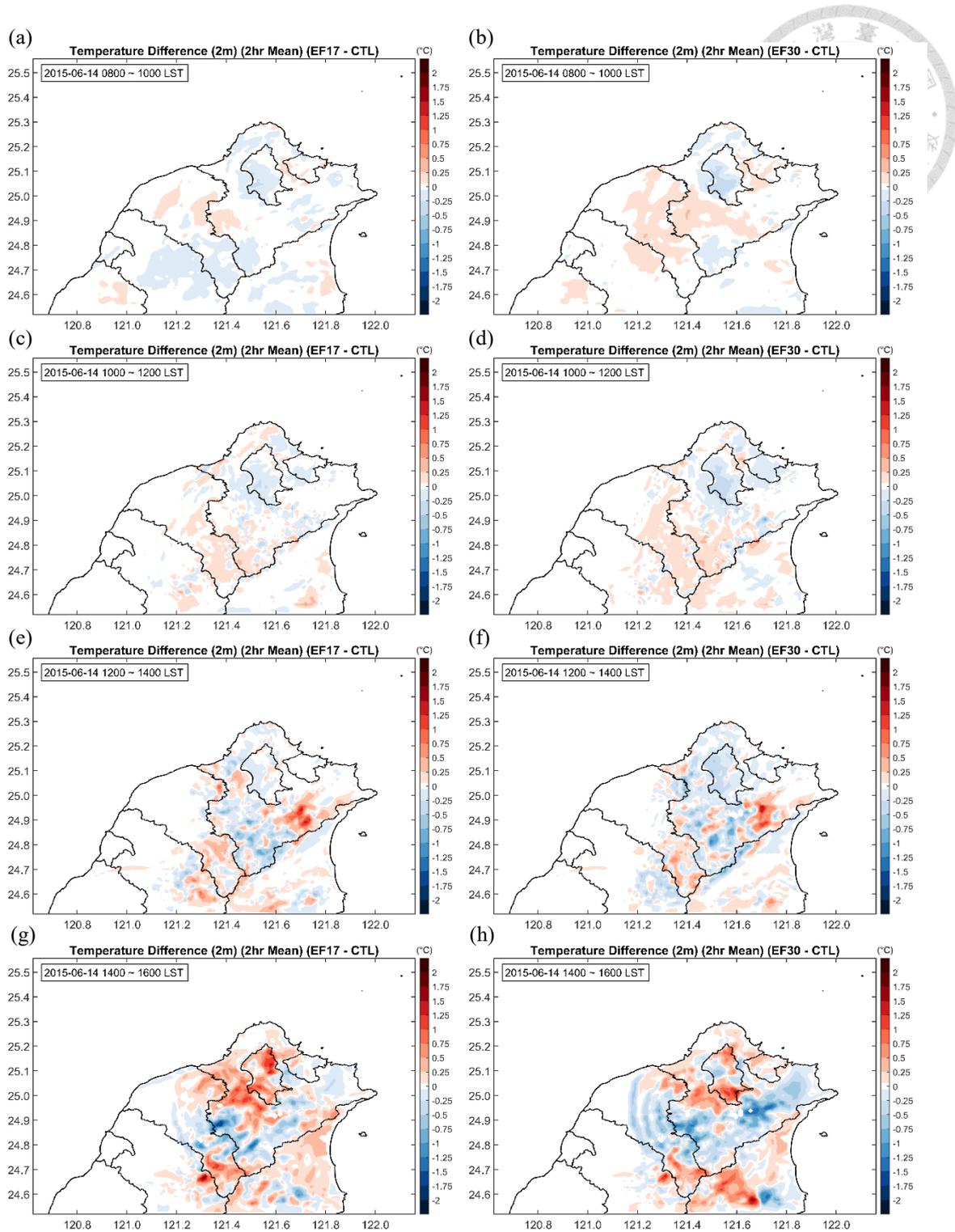
FIG. 3-4. The time evolution of the 2-m temperature difference (2-hr mean). The left column (a), (c), (e) and (g) are for the EF17 and the CTL runs; the right (b), (d), (f) and (h) are for the EF30 and the CTL runs.
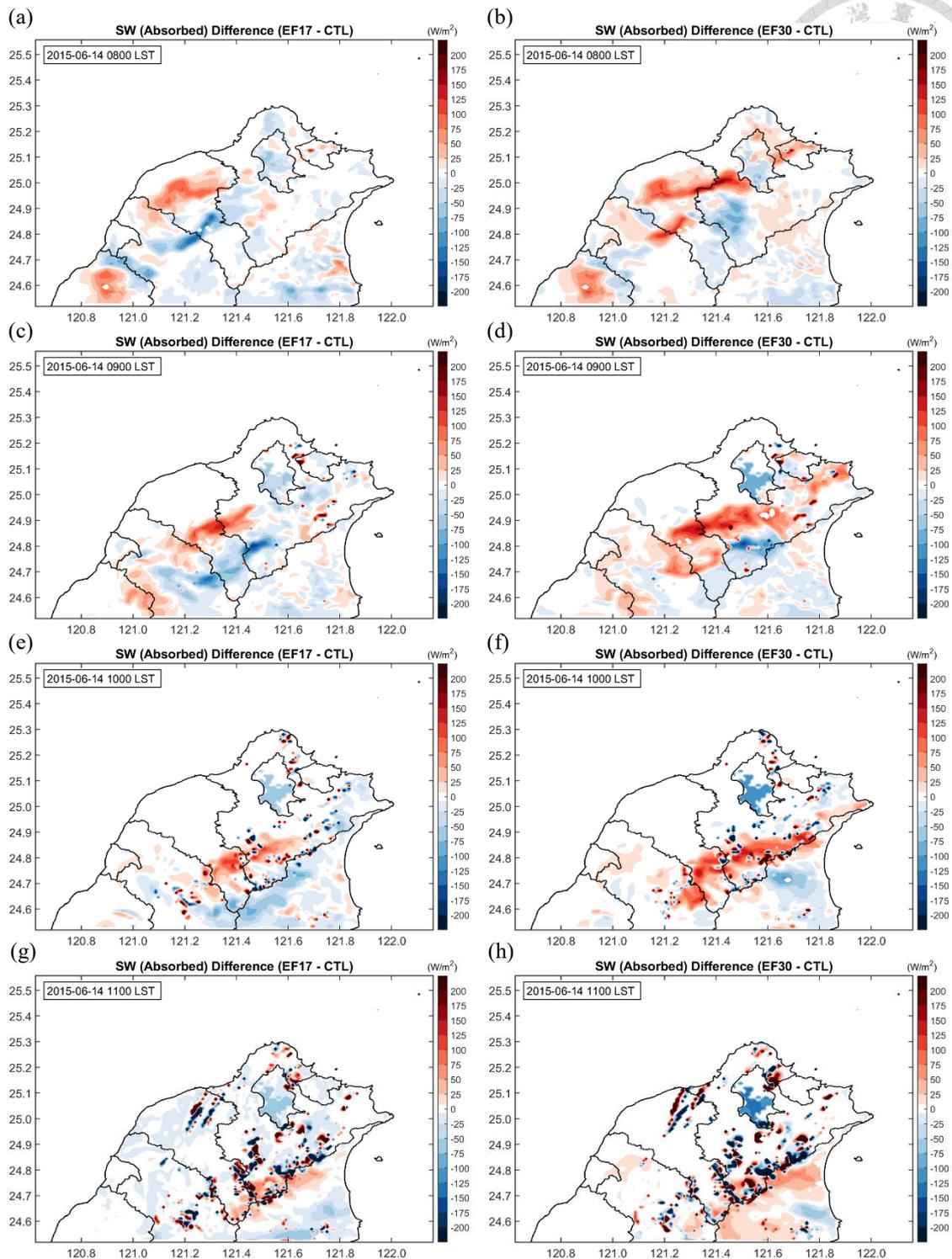
FIG. 3-5. The time evolution of the absorbed SW difference from 0800 ~ 1100 LST. The left column (a), (c), (e) and (g) are for the EF17 and the CTL runs; the right (b), (d), (f) and (h) are for the EF30 and the CTL runs.
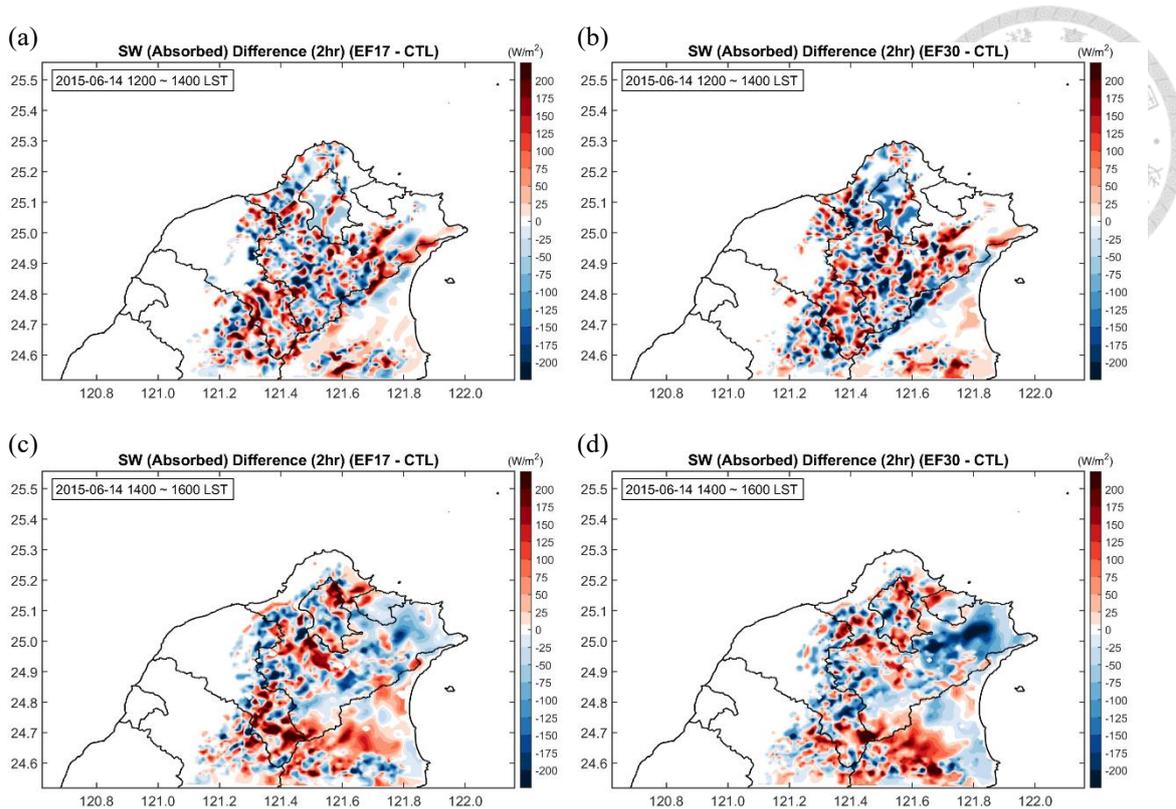
FIG. 3-6. The time evolution of the absorbed SW difference (2-hr mean). The left column (a) and (c) are for the EF17 and the CTL runs; the right (b) and (d) are for the EF30 and the CTL runs.
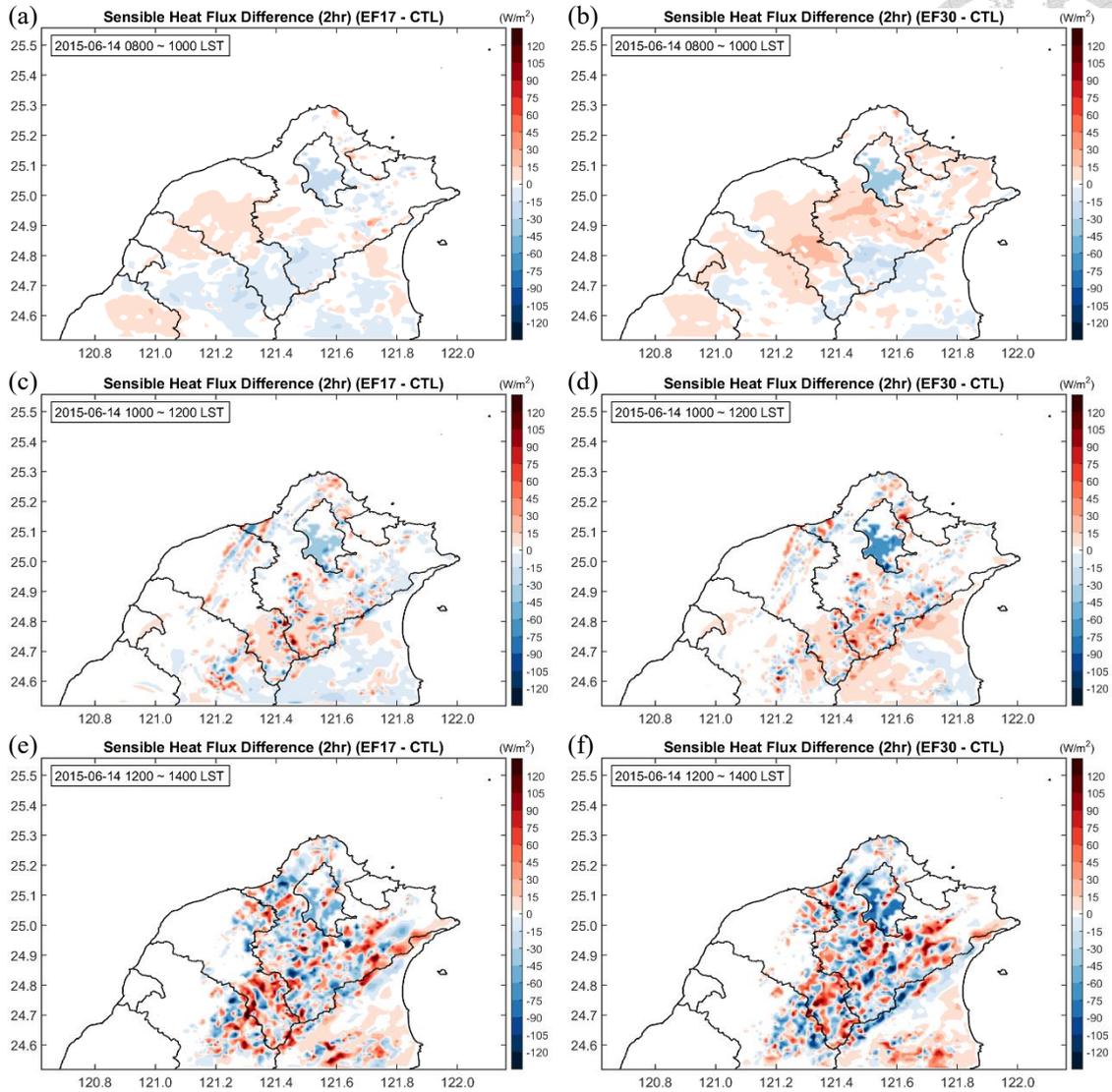
FIG. 3-7. The time evolution of the sensible heat flux difference from 0800 ~ 1400 LST. The left column (a), (c), and (e) are for the EF17 and the CTL runs; the right (b), (d), and (f) are for the EF30 and the CTL runs.
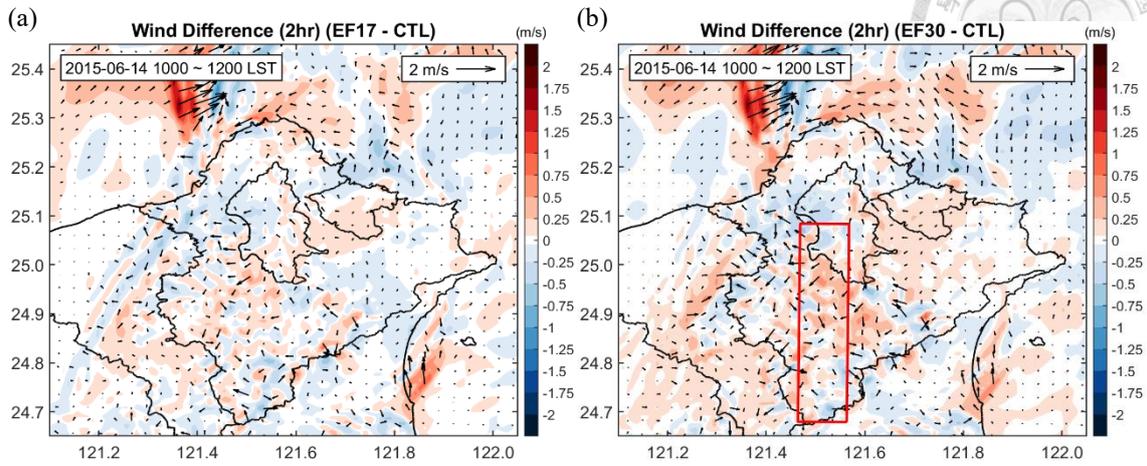
FIG. 3-8.   The 10-m wind difference (2-hr mean), the vectors for wind vectors and the shading for the wind speed.
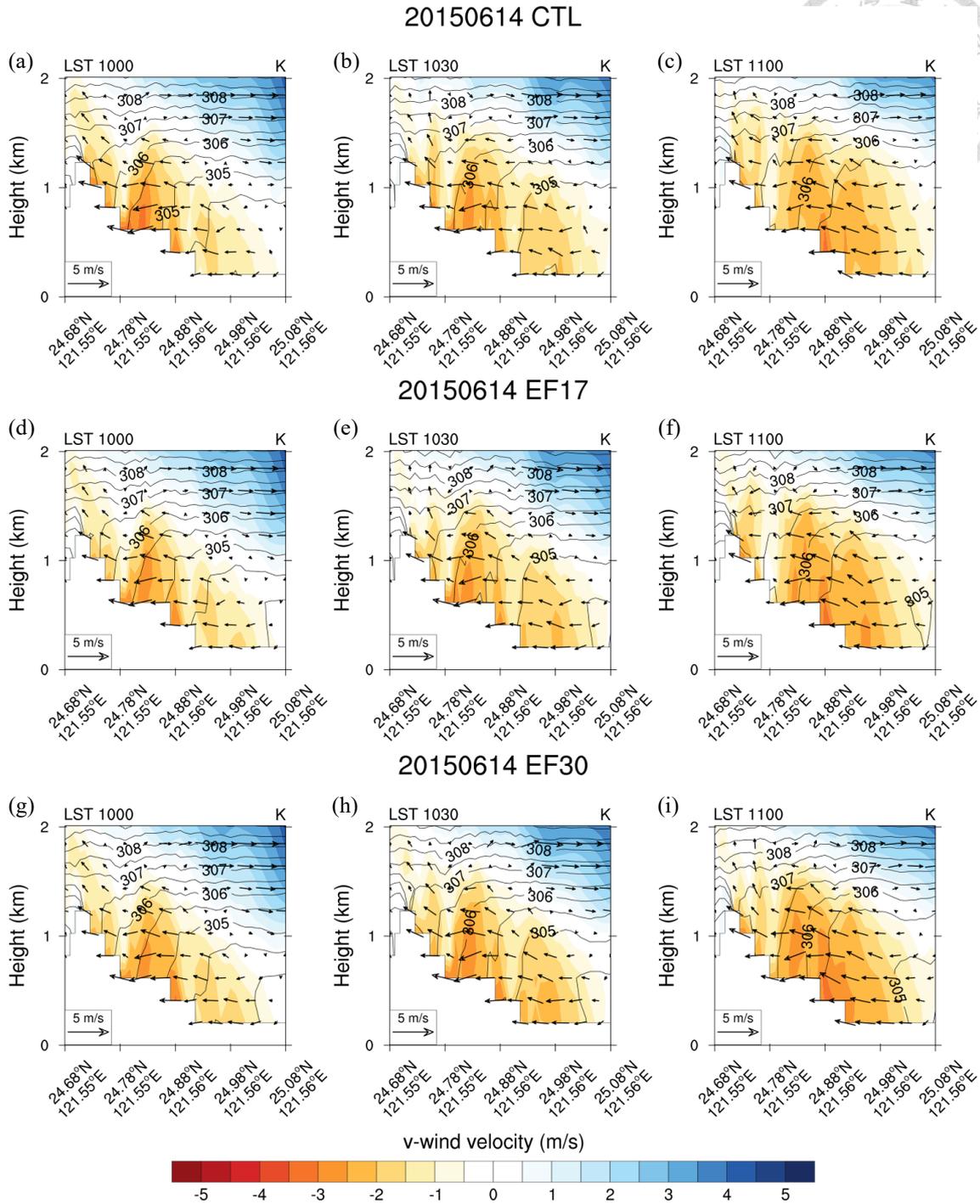
FIG. 3-9. The time evolution of v-wind cross section (the box in FIG. 3-8b) form 1000 ~ 1100 LST, the vectors for the vector sum of v-wind and z-wind, the contours for the potential temperature, and the shading for v-wind velocity. (a), (b) and (c) are for the CTL run; (d), (e) and (f) are for the EF17 run; (g), (h) and (I) are for the EF30 run.
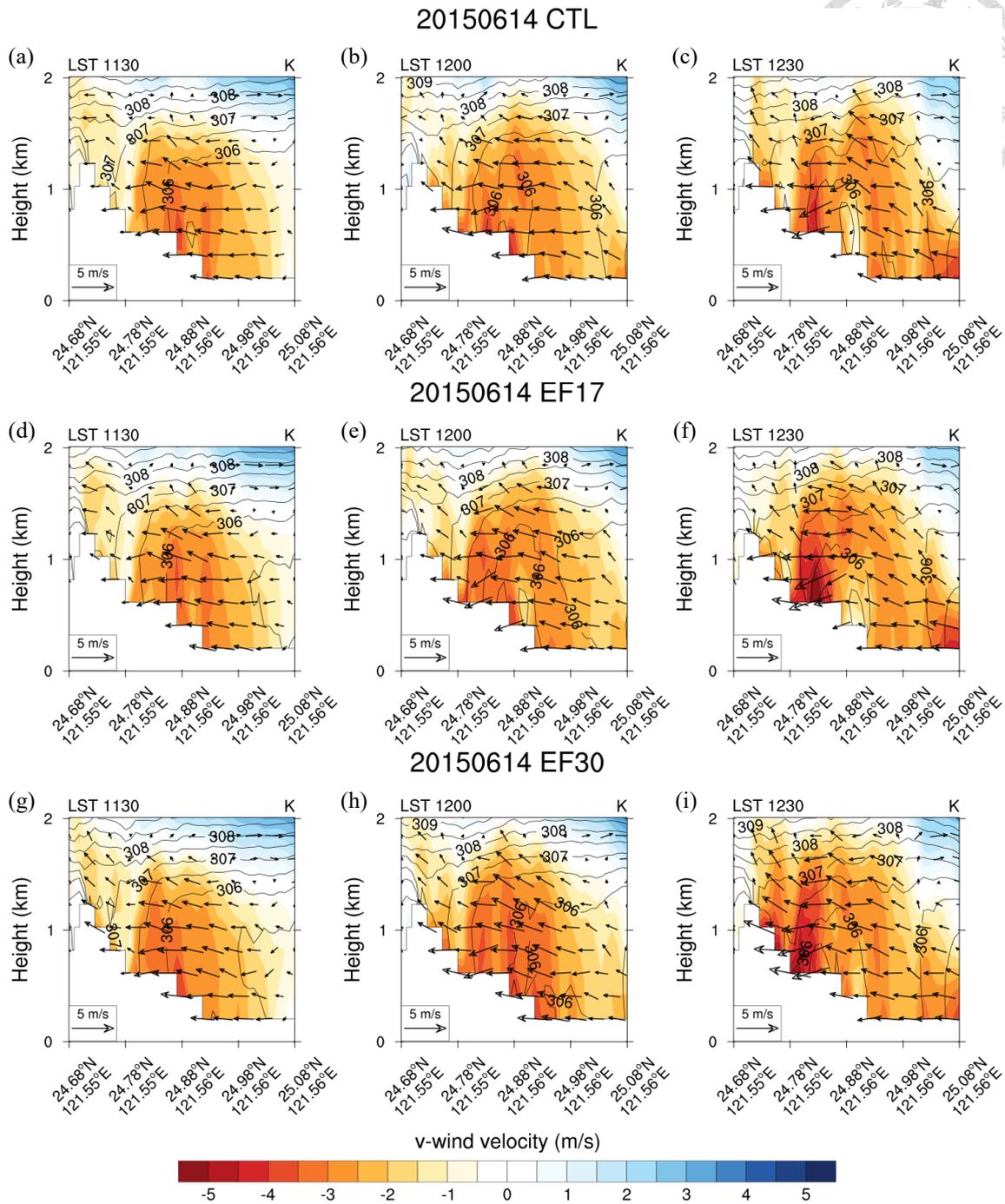
FIG. 3-10. Same as FIG. 3-9, but from 1130 ~ 1230 LST.
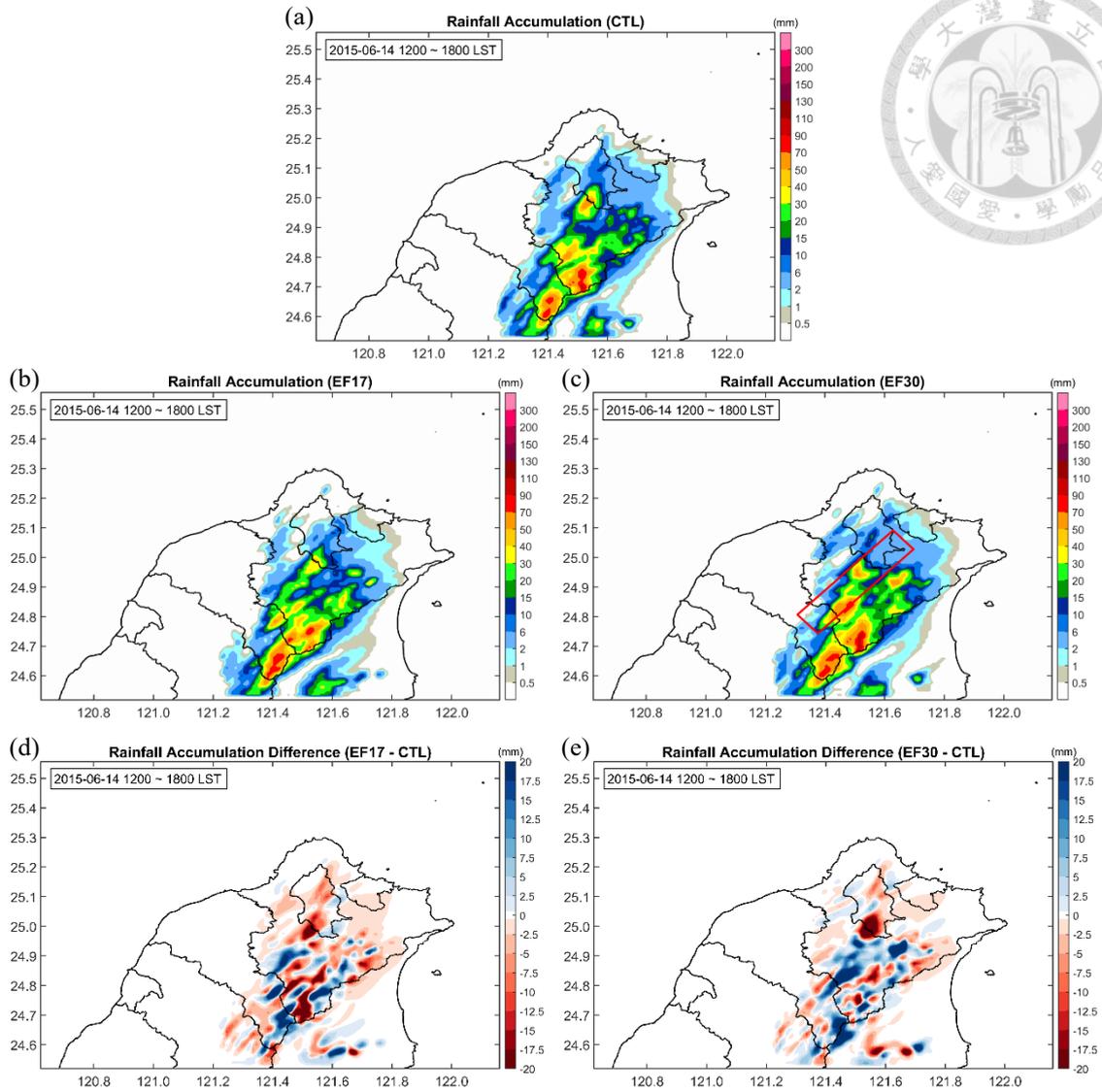
FIG. 3-11. (a), (b) and (c) are the 6-hr accumulated rainfall for the CTL, EF17 and EF30 runs respectively. The vertical cross section in FIG. 3-13 and 3-14 are along the red box in (c). (d) and (e) are the rainfall accumulation difference compared with the CTL run in the EF17 and EF30 runs respectively.

43
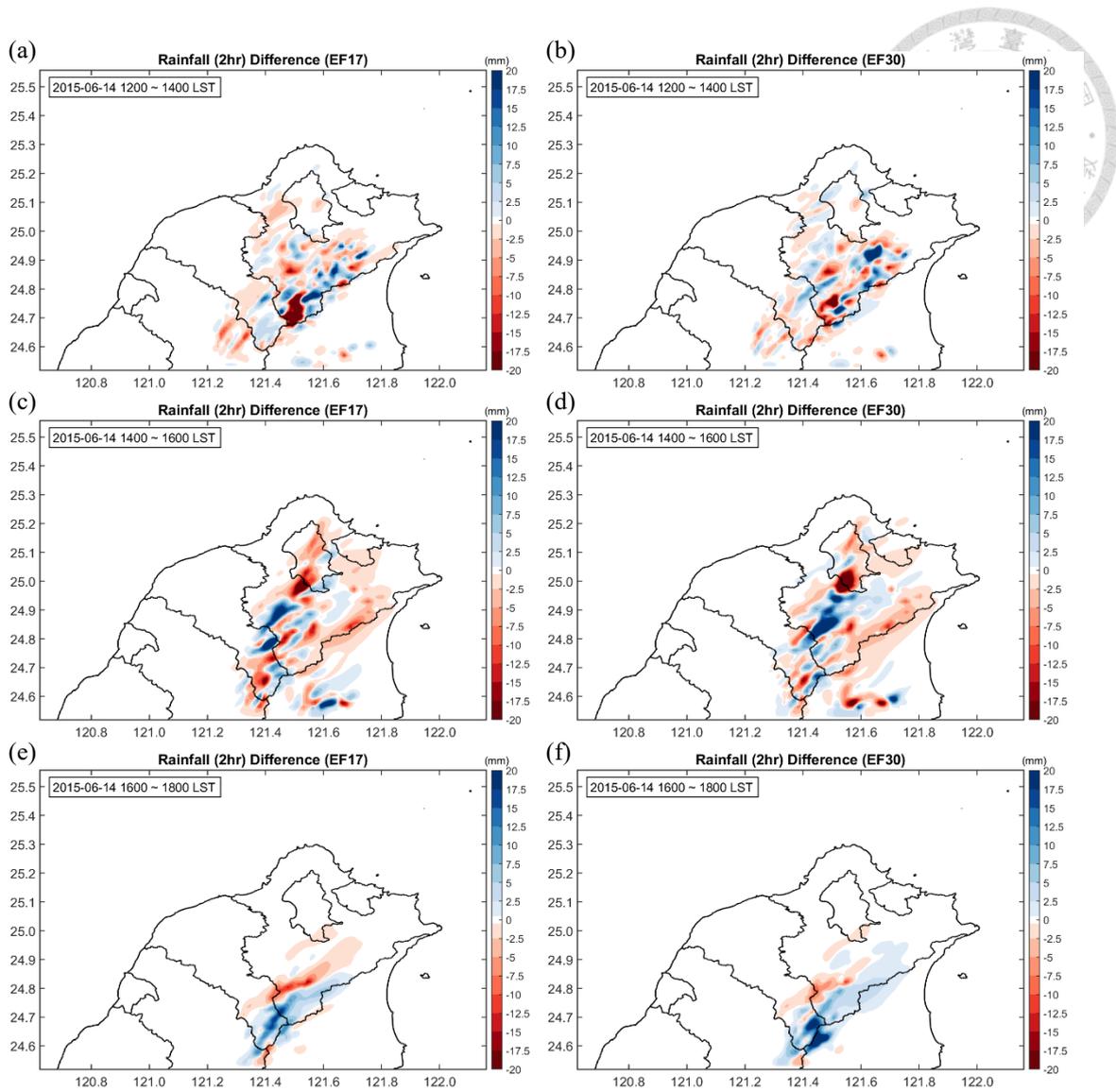
FIG. 3-12. The time evolution of the 2-hr rainfall difference compared with the CTL run from 1200 ~ 1800 LST; (a), (c) and (e) are for the EF17 run; (b), (d) and (f) are for the EF30 run.
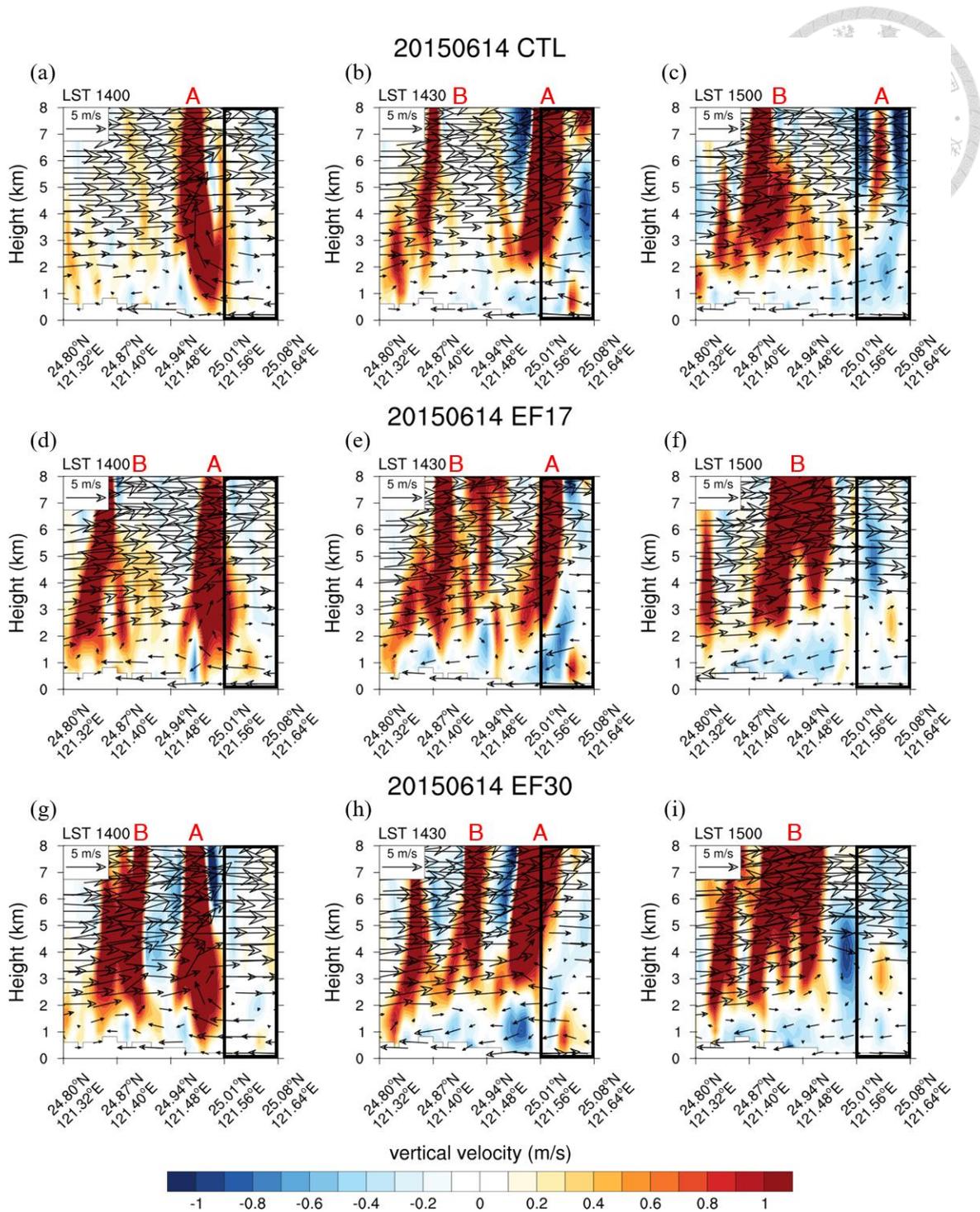
FIG. 3-13. The vertical cross section of the z-winds along the red box in FIG. 3-11c (from 1400 ~ 1500 LST), the vectors for the vector sum of the horizontal winds along the cross section in FIG. 3-11c and the z-winds, the shading for the vertical velocity. (a), (b) and (c) are for the CTL run; (d), (e) and (f) are for the EF17 run; (g), (h) and (i) are for the EF30 run (the Taipei City is marked in the black box).

45
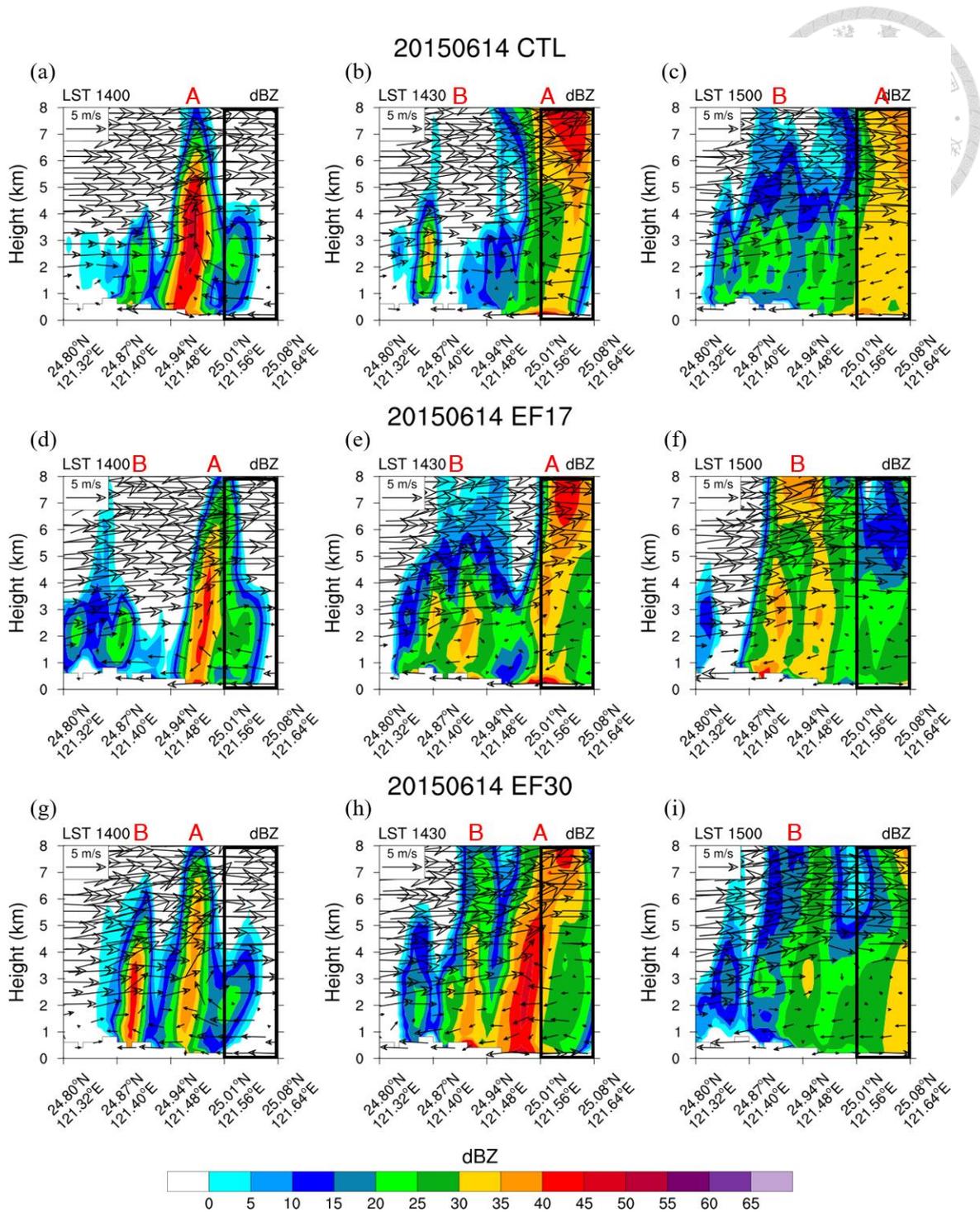
FIG. 3-14. The vertical cross section of the radar reflectivity along the red box in FIG. 3-11c

(from 1400 ~ 1500 LST), the vectors for the vector sum of the horizontal winds

along the cross section in FIG. 3-11c and the z-winds, the shading for the vertical

velocity. (a), (b) and (c) are for the CTL run; (d), (e) and (f) are for the EF17 run;

(g), (h) and (i) are for the EF30 run (the Taipei City is marked in the black box).
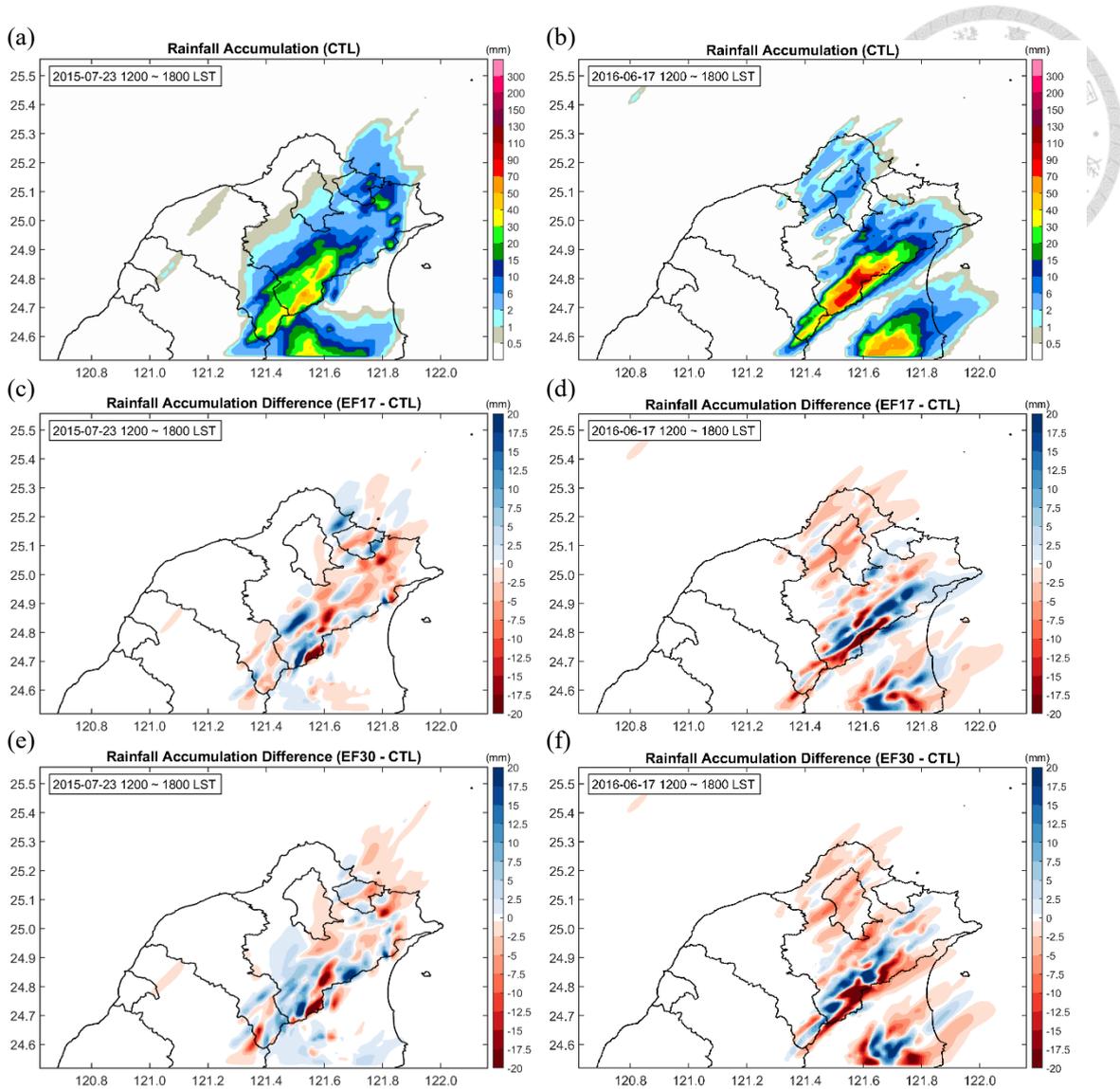
FIG. 4-1. (a), (c) and (e) are the 6-hr accumulated rainfall for the CTL, the rainfall difference compared to the CTL run for the EF17 and EF30 runs respectively in the 23 July 2015 case. The (b), (d) and (f) are the 6-hr accumulated rainfall for the CTL, the rainfall difference compared to the CTL run for the EF17 and EF30 runs respectively in the 16 June 2016 case.
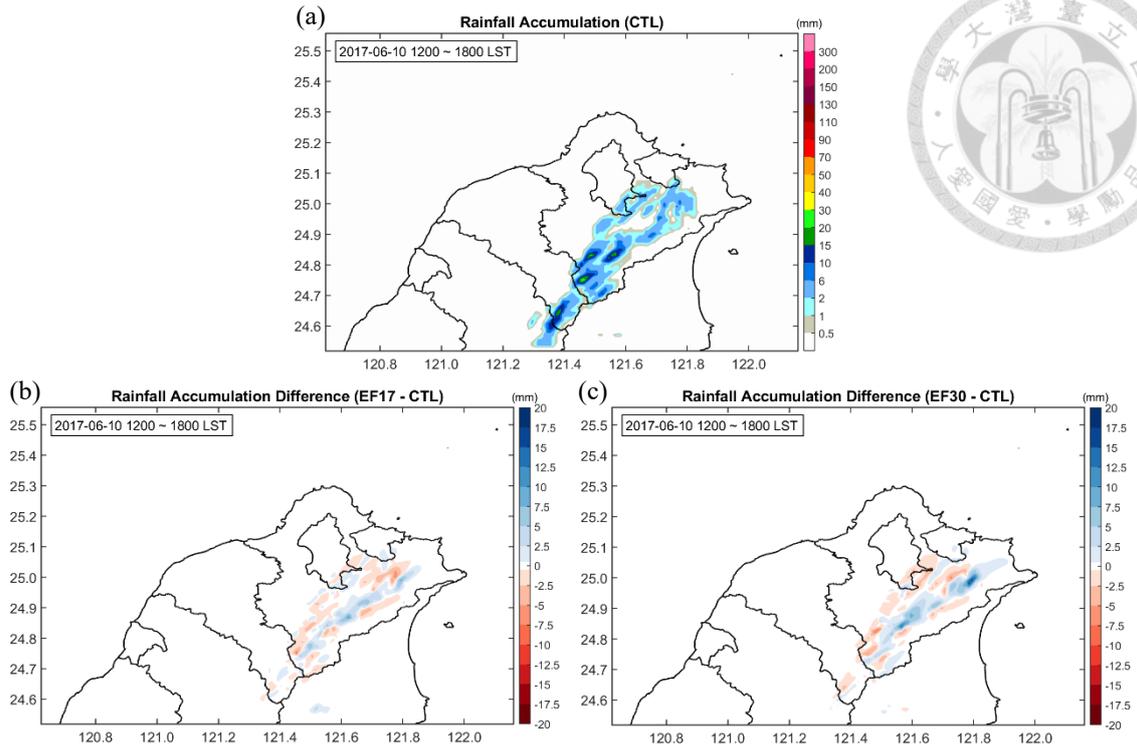
FIG. 4-2. (a), (b) and (c) are the 6-hr accumulated rainfall for the CTL, the rainfall difference compared to the CTL run for the EF17 and EF30 runs respectively in the 10 June 2017 case.

REFERENCE

朱韻雅 (2019)。北台灣午後對流的強降雨事件發展機制。國立臺灣大學大氣科學研究所碩士論文，台北市。 取自 https://hdl.handle.net/11296/jmpj7k

呂罡銘 (2011)。 應用衛星遙測技術解析都市土地覆蓋與地表輻射熱平衡之關係。國立成功大學建築學系碩博士班博士論文，台南市。 取自 https://hdl.handle.net/11296/8njpy6

周仲島, 高聿正, 修榮光, 鍾吉俊, 李宗融,& 郭鴻基 (2016)。 臺北都會區豪雨型午後雷暴的觀測特徵與預報挑戰: 2015 年 6 月 14 日個案研究. 大氣科學, 44(1), 57-82.

經濟部能源局 Bureau of Energy, Ministry of Economic Affairs (n. d.),太陽光電模組產品登錄- PV Module Product Registration. Retrieved May 5, 2019, from https://www.tcpv.org.tw/Product/

經濟部標準檢驗局 Bureau of Standards, Metrology and Inspection, MOEA (2019). 台灣高效能太陽光電模組技術規範, PV TAIWAN Plus Technical Specification.

臺北市政府資訊局 Department of Information Technology, Taipei City Government (n. d.), 臺北市自動化 3D 近似建物模型。 取自 https://github.com/sheethub/tpe3d

Balenzategui, J. L., & Chenlo, F. (2005). Measurement and analysis of angular response of bare and encapsulated silicon solar cells. Solar Energy Materials and Solar Cells, 86(1), 53-83.

Barron-Gafford, G. A., Minor, R. L., Allen, N. A., Cronin, A. D., Brooks, A. E., & Pavao-Zuckerman, M. A. (2016). The Photovoltaic Heat Island Effect: Larger solar power plants increase local temperatures. Scientific reports, 6, 35070.
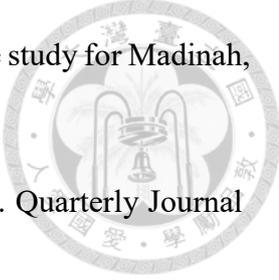
Benghanem, M. (2011). Optimization of tilt angle for solar panel: Case study for Madinah, Saudi Arabia. Applied Energy, 88(4), 1427-1433.

Charney, J. G. (1975). Dynamics of deserts and drought in the Sahel. Quarterly Journal of the Royal Meteorological Society, 101(428), 193-202.

Charney, J., Quirk, W. J., Chow, S. H., & Kornfield, J. (1977). A comparative study of the effects of albedo change on drought in semi–arid regions. Journal of the atmospheric sciences, 34(9), 1366-1385.

Chen, F., Kusaka, H., Tewari, M., Bao, J. W., & Hirakuchi, H. (2004). Utilizing the coupled WRF/LSM/Urban modeling system with detailed urban classification to simulate the urban heat island phenomena over the Greater Houston area. In Fifth Symposium on the Urban Environment (Vol. 2004, pp. 9-11). American Meteorological Society Vancouver, BC, Canada.

Chen, J., Chen, J., Liao, A., Cao, X., Chen, L., Chen, X., He, C., Han, G., Lu, M., Mills, J. Peng, S., Tong, X. & Zhang, W. (2015). Global land cover mapping at 30 m resolution: A POK-based operational approach. ISPRS Journal of Photogrammetry and Remote Sensing, 103, 7-27.

Chen, T. C., Wang, S. Y., & Yen, M. C. (2007). Enhancement of afternoon thunderstorm activity by urbanization in a valley: Taipei. Journal of Applied Meteorology and Climatology, 46(9), 1324-1340.

Haklay, M., & Weber, P. (2008). Openstreetmap: User-generated street maps. IEEE Pervasive Computing, 7(4), 12-18.

Kusaka, H., Kondo, H., Kikegawa, Y., & Kimura, F. (2001). A simple single-layer urban canopy model for atmospheric models: Comparison with multi-layer and slab models. Boundary-layer meteorology, 101(3), 329-358.

Kusaka, H., & Kimura, F. (2004). Coupling a single-layer urban canopy model with a
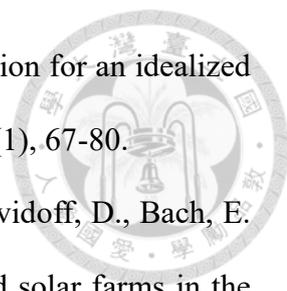
simple atmospheric model: Impact on urban heat island simulation for an idealized case. Journal of the Meteorological Society of Japan. Ser. II, 82(1), 67-80.

Li, Y., Kalnay, E., Motesharrei, S., Rivas, J., Kucharski, F., Kirk-Davidoff, D., Bach, E. & Zeng, N. (2018). Climate model shows large-scale wind and solar farms in the Sahara increase rain and vegetation. Science, 361(6406), 1019-1022.

Lin, C. Y., Chen, W. C., Chang, P. L., & Sheng, Y. F. (2011). Impact of the urban heat island effect on precipitation over a complex geographic environment in northern Taiwan. Journal of Applied Meteorology and Climatology, 50(2), 339-353.

Masson, V., Bonhomme, M., Salagnac, J. L., Briottet, X., & Lemonsu, A. (2014). Solar panels reduce both global warming and urban heat island. Frontiers in Environmental Science, 2, 14.

Meral, M. E., & Dincer, F. (2011). A review of the factors affecting operation and efficiency of photovoltaic based electricity generation systems. Renewable and Sustainable Energy Reviews, 15(5), 2176-2184.

Miao, J. E., & Yang, M. J. (2020). A modeling study of the severe afternoon thunderstorm event at Taipei on 14 June 2015: The roles of sea breeze, microphysics, and terrain. Journal of the Meteorological Society of Japan. Ser. II.

Nemet, G. F. (2009). Net radiative forcing from widespread deployment of photovoltaics. Environmental science & technology, 43(6), 2173-2178.

Parretta, A., Sarno, A., Tortora, P., Yakubu, H., Maddalena, P., Zhao, J., & Wang, A. (1999). Angle-dependent reflectance measurements on photovoltaic materials and solar cells. Optics Communications, 172(1-6), 139-151.

Scherba, A., Sailor, D. J., Rosenstiel, T. N., & Wamser, C. C. (2011). Modeling impacts of roof reflectivity, integrated photovoltaic panels and green roof systems on sensible heat flux into the urban environment. Building and Environment, 46(12), 2542-2551.
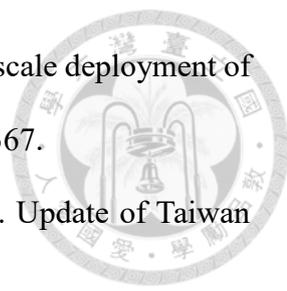
Taha, H. (2013). The potential for air-temperature impact from large-scale deployment of solar photovoltaic arrays in urban areas. Solar Energy, 91, 358-367.

Tai, L. H., Hong, J. S., Tsuang, B. J., Tsai, J. L., & Ni, P. J. (2008). Update of Taiwan land-use data in WRF model. J. Atmos. Sci, 36, 43-61.

Yang, H., & Lu, L. (2007). The optimum tilt angles and orientations of PV claddings for building-integrated photovoltaic (BIPV) applications.